Understanding the interactions between vibrational modes and excited state relaxation in $Y_{3-x}Ce_xAl_5O_{12}$: design principles for phosphors based on 5*d*–4*f* transitions

Yuan-Chih Lin, Paul Erhart, Marco Bettinelli,
Nathan C. George, Stewart F. Parker and Maths Karlsson

Published version information

Citation: Y Lin et al. "Understanding the interactions between vibrational modes and excited state relaxation in $Y_{3-x}Ce_xAl_5O_{12}$: design principles for phosphors based on 5*d*–4*f* transitions." Chemistry of Materials, vol. 30, no. 6 (2018): 1865-1877.

DOI: 10.1021/acs.chemmater.7b04348

Understanding the Interactions Between Vibrational Modes and Excited State Relaxation in $Y_{3-x}Ce_xAl_5O_{12}$: Design Principles for Phosphors Based on 5*d*–4*f* Transitions

Yuan-Chih Lin,[†] Paul Erhart,[‡] Marco Bettinelli,[¶] Nathan C. George,[§,⊥] Stewart F. Parker,[⊥] and Maths Karlsson[*,†]

† *Department of Chemistry and Chemical Engineering, Chalmers University of Technology, SE-412 96 Göteborg, Sweden*

‡ *Department of Physics, Chalmers University of Technology, SE-412 96 Göteborg, Sweden*

¶ *Luminescent Materials Laboratory, University of Verona and INSTM, UdR Verona, 37134 Verona, Italy*

§ *Department of Chemical Engineering, University of California, Santa Barbara, California 93106, United States*

⊥ *Mitsubishi Chemical Center for Advanced Materials, University of California, Santa Barbara, California 93106, United States*

⊥ *ISIS Facility, STFC Rutherford Appleton Laboratory, Chilton, Didcot, Oxon OX11 0QX United Kingdom*

E-mail: maths.karlsson@chalmers.se

Abstract

The oxide garnet $Y_3Al_5O_{12}$ (YAG), when a few percent of the activator ions Ce^{3+} substitutes for Y^{3+}, is a luminescent material widely used in phosphor-converted white

lighting. However, fundamental questions surrounding the defect chemistry and luminescent performance of this material remain, especially in regard to the nature and role of vibrational dynamics. Here, we provide a complete phonon assignment of YAG and establish the general spectral trends upon variation of the Ce^{3+} dopant concentration and temperature, which are shown to correlate with the macroscopic luminescence properties of $Y_{3-x}Ce_xAl_5O_{12}$. Increasing the Ce^{3+} concentration and/or temperature leads to a red-shift of the emitted light, as a result of increased crystal-fi splitting due to a larger tetragonal distortion of the CeO_8 moieties. Decreasing the Ce^{3+} concentration or co-substitution of smaller and/or lighter atoms on the Y sites creates the potential to suppress thermal quenching of luminescence because phonon modes important for non-radiative relaxation mechanisms are upward-shifted and hence less readily activated. It follows that design principles for finding new Ce^{3+} doped oxide phosphors emitting at longer wavelengths require tetragonally distorted environments around the CeO_8 moieties, and a sufficiently rigid host structure and/or low activator-ion concentration to avoid thermal quenching of luminescence.

Keywords

phosphor, LED, phonon, luminescence, garnet

INTRODUCTION

Phosphor-converted white light emitting diodes (pc-WLEDs) are efficient light sources used in lighting, high-tech displays, and electronic devices. The most widely used type of pc-WLEDs is composed of an (In,Ga)N-based blue LED that is used to excite either a yellow phosphor or a combination of phosphors resulting in the emission of white light. The phosphors usually consist of a crystalline host material containing a small amount of activator ions that serve as luminescent centers. ~~Although the activator ions have intrinsic characteristics~~

~~that are essential to the luminescence properties of phosphors, the static and dynamic structure of the host material around the activator ions ultimately determines phosphor performance, such as color and luminous efficacy, emission lifetime, and thermal stability.[1-3]~~ Of specific concern for this work is cerium-doped yttrium aluminum garnet ($Y_{3-x}Ce_xAl_5O_{12}$, $YAG:Ce^{3+}$), which is widely considered as the most important phosphor for pc-WLEDs.[1–6] The YAG structure can be described in terms of a 160-atom body-centered cubic unit cell (80 atoms in the primitive cell) of the O_h^{10} ($Ia\bar{3}d$) space group.[7] The primitive cell comprises four $Y_3Al^{VI}_2(Al^{IV}O_4)_3$ units, where the superscripts VI and IV refer to octahedral and tetrahedral coordination, respectively. Therefore, there are two sites for the Al atoms: Al^{VI} occupies Wyckoff position 8(a) with S_6 site symmetry, whereas Al^{IV} occupies Wyckoff position 12(d) with S_4 site symmetry. The AlO_4 and AlO_6 moieties can be regarded as slightly distorted tetrahedra and octahedra, respectively,[8] and approximately assigned to the point group symmetry of regular tetrahedra and octahedra, T_d and O_h, respectively. The O atoms occupy Wyckoff position 48(h) with C_1 site symmetry and each O atom is shared with two YO_8 moieties, one AlO_6 moiety, and one AlO_4 moiety. The Y^{3+} ions are situated at Wyckoff position 12(c) with D_2 site symmetry. Each Y^{3+} ion is dodecahedrally coordinated to eight O atoms that are shared with the neighboring two AlO_4 tetrahedra and four AlO_6 octahedra (Figure 1). The YO_8 dodecahedra are tetragonally distorted, resulting in two different Y-O distances (d_1 and d_2 in Figure 1).[9–11] The degree of tetragonal distortion, which may be tuned *via* methods such as cation substitution on the Al sites as in $Y_3Al_{5-y}Ga_yO_{12}:Ce^{3+}$,[9,12] has been shown to correlate with a shift of the emission spectrum towards longer wavelengths (red-shift) and is therefore likely to be an important local structural property for the lighting characteristics of garnet type phosphors. Furthermore, recent results obtained from neutron and X-ray total scattering experiments combined with reverse Monte-Carlo (RMC) modeling, X-ray absorption spectroscopy, and nuclear magnetic resonance (NMR) studies, suggest that the Ce^{3+} doping leads to pronounced local structural disorder and softening of the crystal structure, which correlates with a decrease in the emission intensity of the emitted

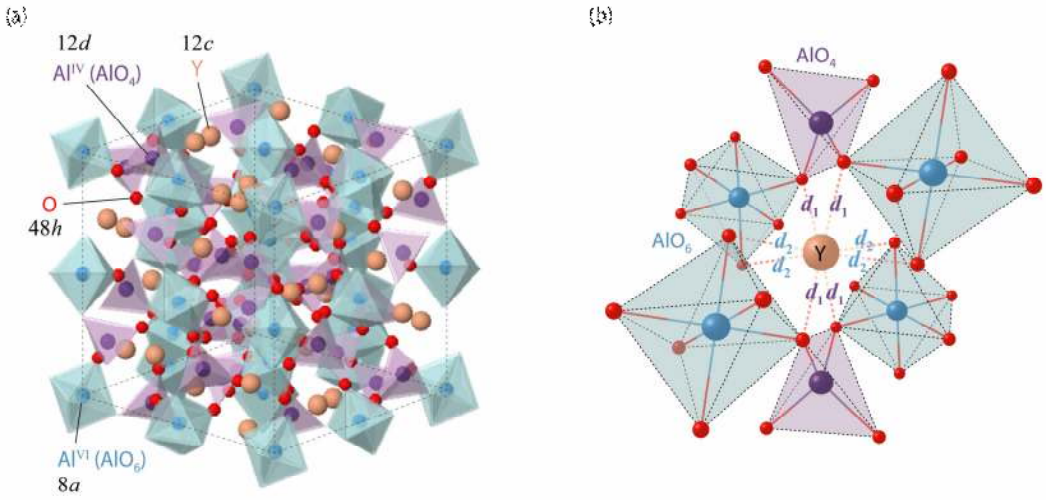

Figure 1: (a) Schematic illustration of the unit cell of YAG, with the tetrahedral AlO_4 moieties distinguished in purple and the octahedral AlO_6 moieties distinguished in turquoise. Y atoms occupy Wyckoff position 12(*c*) and are dodecahedrally coordinated with eight nearest oxygens that are shared between two AlO_4 tetrahedra and four AlO_6 octahedra. Octahedrally coordinated Al^{VI}, tetrahedrally coordinated Al^{IV}, and O atoms are situated at Wyckoff positions 8(*a*), 12(*d*), and 48(*h*), respectively. (b) A close-up of the local coordination of an Y atom. The atomic distances of the first shell (Y–O) and the second shell (Y–O) are labeled by d_1 and d_2 respectively.

light.[11] However, as opposed to these previous studies, which have been primarily focused on the relationship between static structure and light-emitting characteristics, few studies have focused on the role of the dynamic structure, *i.e.* the vibrational dynamics at and near the activator ion sites, on the macroscopic luminescence properties of $YAG:Ce^{3+}$. In particular, while previous vibrational spectroscopy studies of garnet type oxides, *e.g.*, by Raman and infrared (IR) spectroscopy,[8,13–17] group-theoretical predictions,[8,18] and theoretical calculations,[16,19,20] have provided important information of the vibrational dynamics in YAG and its doped variants, including the assignment of optically active phonon normal modes,[8,15–20] no study has provided a complete phonon assignment in terms of the vibrational amplitudes of the motions of the individual AlO_4, AlO_6, and YO_8 moieties which constitute the garnet structure. ~~There are several vibrational spectroscopy studies of garnet type oxides,~~ *e.g.*, by Raman and infrared (IR) spectroscopy, [8,13–17] group-theoretical predictions, [8,18]

and theoretical calculations, ,[16,19,20] which have provided important information, including the assignment as well as the frequencies of optically active phonon normal modes.[8,15–20] However, no study has provided a complete phonon assignment in terms of the vibrational amplitudes of the motions of the individual AlO_4, AlO_6, and YO_8 moieties which constitute the garnet structure. Furthermore, due to the low Raman scattering cross section for some of the (in principle) Raman-active modes, not all group-theoretically predicted modes have been experimentally identified to date. Additionally, the optically-silent modes in YAG that might be observable with other techniques, such as inelastic neutron scattering (INS), have not been studied before. By studying these properties, we, in this work, aim to decompose each phonon normal mode into the individual motions of AlO_4, AlO_6, and YO_8 moieties, to determine how the spectral features depend on both Ce^{3+} concentration and temperature, as well as to investigate to what extent the vibrational dynamics may be manipulated as a means for optimizing luminescence properties, such as color and intensity of the emitted light. To this end, we present a systematic analysis of the vibrational dynamics in $Y_{3-x}Ce_xAl_5O_{12}$, as a function of Ce^{3+} concentration (x = 0–0.09) and temperature (T = 80–870 K), using a combination of Raman and IR spectroscopy, INS, and *ab-initio* calculations based on density functional theory (DFT). By analyzing experimental and computed vibrational spectra we provide a complete assignment of the vibrational modes and establish the general spectral trends as a function of Ce^{3+} dopant concentration and temperature, which are shown to correlate with the color and intensity of the emitted light excellent luminescence properties of YAG:Ce^{3+}. Since our results are the consequence of the symmetry relations intrinsic to the garnet structure, our findings can be expected to be generally applicable to materials of this type and thereby provide a route for tuning optical properties, such as light emitting color and intensity, that depend strongly on the static and dynamic structure of the host material around the luminescent centers in phosphors based on 5*d*-4*f* transitions. Moreover, similar matters concerning the local structures near substituent ions are important to the properties of other oxides used as thermoelectrics,[21] multiferroics,[22] proton conductors,[23]

and in photovoltaic applications.[24]

EXPERIMENTAL

Sample Preparation

Samples of $Y_{3-x}Ce_xAl_5O_{12}$ with $x = 0$, 0.03, 0.06, and 0.09 (YAG, YAG:1%Ce^{3+}, YAG:2%Ce^{3+}, and YAG:3%Ce^{3+}, respectively), were prepared using conventional solid-state preparation methods. Starting materials consisting of stoichiometric amounts of Y_2O_3 (Sigma-Aldrich, 99.9% purity), Al_2O_3 (Sumitomo AKP-50, 99.99% purity), and CeO_2 (Cerac, 99.9% purity), were ground with an agate mortar and pestle, placed in alumina crucibles, and fired at 1600 °C for 96 h in an alumina tube furnace under a 0.2 L/min gas flow of 5% H_2/N_2. After the starting materials had reacted, the phosphor cakes were ground with an agate mortar and pestle into fine powders. Further details of the sample preparation and characterization can be found in ref. 11.

Infrared Spectroscopy

IR spectra were measured in transmittance over the range 50–900 cm^{-1} using a Bruker IFS 66v/s spectrometer equipped with a deuterated-triglycine sulfate detector and exchangeable beam splitters; a Mylar 6 beam splitter was used for the range 30–680 cm^{-1} (far-IR) and a KBr beam splitter for the range 370–900 cm^{-1} (mid-IR). The powder samples were homogeneously dispersed to ≈2–5 wt% in 0.1 g of polyethylene (PE) powder and 0.1 g KBr powder, respectively, and thereafter pressed into cylindrical pellets under a load of 7 tons. These pellets were subsequently used for measurements in the far-IR (PE pellets) and mid-IR (KBr pellets) range, respectively. Spectra of pure PE and KBr pellets were used as reference spectra. Absorbance-like spectra were derived by taking the logarithm of the ratio of reference and sample spectra.

High-temperature IR spectra (300–780 K) were recorded using a heating block attached

to the sample chamber module of the Bruker IFS 66v/s spectrometer, and with a pellet containing 0.24 wt% of sample (YAG or $YAG:Ce^{3+}$) in 0.45 g CsI. The reason for using CsI rather than PE and KBr matrix materials for these measurements is related to the fact that PE melts at around 400 K and KBr is too absorbent below approximately 370 cm^{-1}. The use of CsI pellets, however, comes at the expense of a cutoff at approximately 125 cm^{-1} compared to about 4 cm^{-1} for PE. Therefore, the lowest-frequency part of the spectrum, 50–125 cm^{-1}, was not accessible during the high-temperature measurements.

Raman Spectroscopy

The Raman spectroscopy measurements were performed on two different instruments. The measurements on the undoped material, YAG, were performed on a DILOR XY-800 spectrometer equipped with a CCD detector, in a double subtractive grating configuration. Spectra were measured over the range 75–900 cm^{-1} using the 514 nm line from an Ar^+/Kr^+ laser and with the light focused on the sample through an optical objective lens. For the measurements at room temperature, we used a long working distance ×40 objective lens and the power on the sample was adjusted to 1.6 mW with a laser spot size on the sample of ≈1 μm in diameter. For the variable temperature measurements (80–870 K), the ×40 objective lens was exchanged for a ×50 objective lens, and the power was increased to 6.8 mW with a laser spot size on the sample of ≈8 μm in diameter. The temperature was controlled using a heating device from Linkam (model THMS 600). All spectra were measured with linearly polarized light impinging on the sample and unpolarized light collected at the CCD.

The measurements on the doped materials, $YAG:z\%Ce^{3+}$ (z = 1–3), were performed using a Bruker MultiRAM FT-Raman spectrometer. Two excitation sources (785 nm and 1064 nm in wavelength with laser power of 500 mW, and 1000 mW, respectively) were used separately to distinguish the Raman-scattering bands from the unwanted electronic peaks in the spectra over the range of 85–900 cm^{-1}. The spectra were measured with a resolution of 2 cm^{-1} (full width at half maximum, FWHM). Each spectrum was recorded with at least

5000 scans and a scan velocity of 5 kHz by liquid N_2 cooled detectors (TE-Si avalanche pin diode and LN-Ge diode for 785-nm and 1064-nm excitation sources, respectively).

Inelastic Neutron Scattering

The INS experiment was performed on the undoped material, YAG, on TOSCA.[25] The sample, weighing approximately 31 grams, was loaded in an aluminum sachet, which was subsequently inserted into a thin-walled aluminum can. The measurement was performed at 15 K for 28 hours.

As opposed to optical vibrational spectroscopy (IR and Raman), INS does not rely on any selection rules, which implies that all 240 phonon modes in YAG are at least in principle accessible. However, the INS intensity depends crucially on the neutron scattering cross section of the constituent atoms. In the case of YAG, the total neutron scattering cross sections of Y, Al, and O are 7.7, 1.5, and 4.2 barns (1 barn = 1×10^{-24} cm^2), respectively, as a result of which the contribution from Al vibrations is relatively weak. Furthermore, while IR and Raman spectra relate to zone-center modes, INS spectroscopy is sensitive to modes at all wavevectors. Generally speaking INS is a two-dimensional form of spectroscopy, since the measured dynamical structure factor $S(Q, \omega)$ depends on both energy transfer (ω) and momentum transfer (Q). However, TOSCA[25] follows a fixed trajectory through (Q, ω) space, such that there is a single Q-value at each energy transfer, (ω).

Photoluminescence Spectroscopy

Emission spectra of the $YAG:z\%Ce^{3+}$ (z = 1, 2, and 3) samples were measured using a UV-VIS spectrometer (USB2000+, Ocean Optics) coupled to an optical fiber with a 495 nm long-pass filter placed in front. A laser (DeltaDiode-450L, HORIBA Scientific) of 454 nm in wavelength with a pulse width of about 80 ps and a repetition rate of 50 MHz was used as the excitation source. Each spectrum was measured at 300 K for 40 ms, and it was averaged over 40 accumulations.

THEORETICAL

Density Functional Theory Calculations

Density functional theory (DFT) calculations were carried out using the projector augmented wave method[26,27] as implemented in the Vienna *ab-initio* simulation package.[28,29] Exchange-correlation effects were treated within the generalized gradient approximation as parameterized by Perdew, Burke, and Ernzerhof (PBE).[30] Ion positions and the cell metric were fully relaxed until all atomic forces were less than 5 meV/Å and absolute stresses below 0.05 kbar. In these calculations, the Brillouin zone of the 80-atom primitive cell was sampled using the Γ-point only and the plane wave basis set was expanded up to a cutoff energy of 600 eV. Subsequently, the force constant matrix was constructed using the finite displacement method with a displacement of 0.015 Å. To achieve highly converged forces, the energy convergence criterion for the electronic self-consistency loop was tightened to 10^{-6} eV, the reciprocal space projection scheme was employed, and an additional support grid was used for the evaluation of the forces. Test calculations using larger cells with up to 320 atoms showed that for the present purpose the 80-atom cell is sufficient. This is related to YAG being a comparably stiff matrix with a correspondingly rather short-ranged force constant matrix.

Phonon Assignment

The phonon normal modes of YAG were obtained by diagonalizing the force constant matrix obtained from DFT calculations and analyzed using the phonopy package[31] as well as in-house Python code. Symmetry analyses were supported by the spglib package.[32] Each normal mode is associated with a vibrational frequency (eigenvalue) and an eigenvector that describes the atomic displacement pattern. In order to characterize each normal mode in terms of the motions of individual AlO_4 tetrahedra, AlO_6 octahedra, and YO_8 dodecahedra, we mapped the extended lattice vibrational modes (phonons) onto a set of localized

(molecular) vibrational modes, following the procedure described in the flowchart shown in Figure 2. To this end, we consider each molecular vibration to be a superposition of (i) inter-molecular (external-mode) motions including translatory (**T**) and rotary (**R**) motion of the whole molecular unit (AlO_4, AlO_6, or YO_8) and (ii) intra-molecular (internal-mode) motions involving stretching (**S**) and bending (**B**) vibrations. Here, **S** and **B** vibrations are expressed using so-called symmetry coordinates, $|\eta\rangle$, that describe atomic vibrations in terms of the internal coordinates Δr (variation in bonding length) and $\Delta\theta$ (variation in bonding angle), respectively.[33,34] Specifically, we employed symmetry coordinates for tetrahedral (AlO_4), octahedral (AlO_6), and cubic (YO_8) moieties, which are illustrated in Figure S1. Strictly speaking, the YO_8 environment possesses only dodecahedral symmetry. It can, however, be thought of as a tetragonally distorted cube, whence for simplicity, here, it was treated as a cubic moiety. A symmetry coordinate $|\eta\rangle$ of a moiety with a point symmetry (*e.g.* T_d for tetrahedral AlO_4, and O_h for octahedral AlO_6 and cubic YO_8) involving variable symmetry operations R can be obtained from[33]

$$|\eta\rangle = \sum_R R \cdot \chi_\eta^R \cdot \Delta s, \tag{1}$$

where χ_η^R is the associated character value and Δs is the variation of the internal coordinates (Δr and $\Delta\theta$) prior to employing the symmetry operation R. In this study, all symmetry coordinates were normalized and degenerate ones were further treated so that they are orthogonal to each set, see Table S1. In other words, a symmetry coordinate may be expressed by any result of a linear combination of the orthogonal sets with the same symmetry, which may be found in ref. 35 for a cube, in ref. 36 for an octahedron, and in ref. 34 for a tetrahedron.

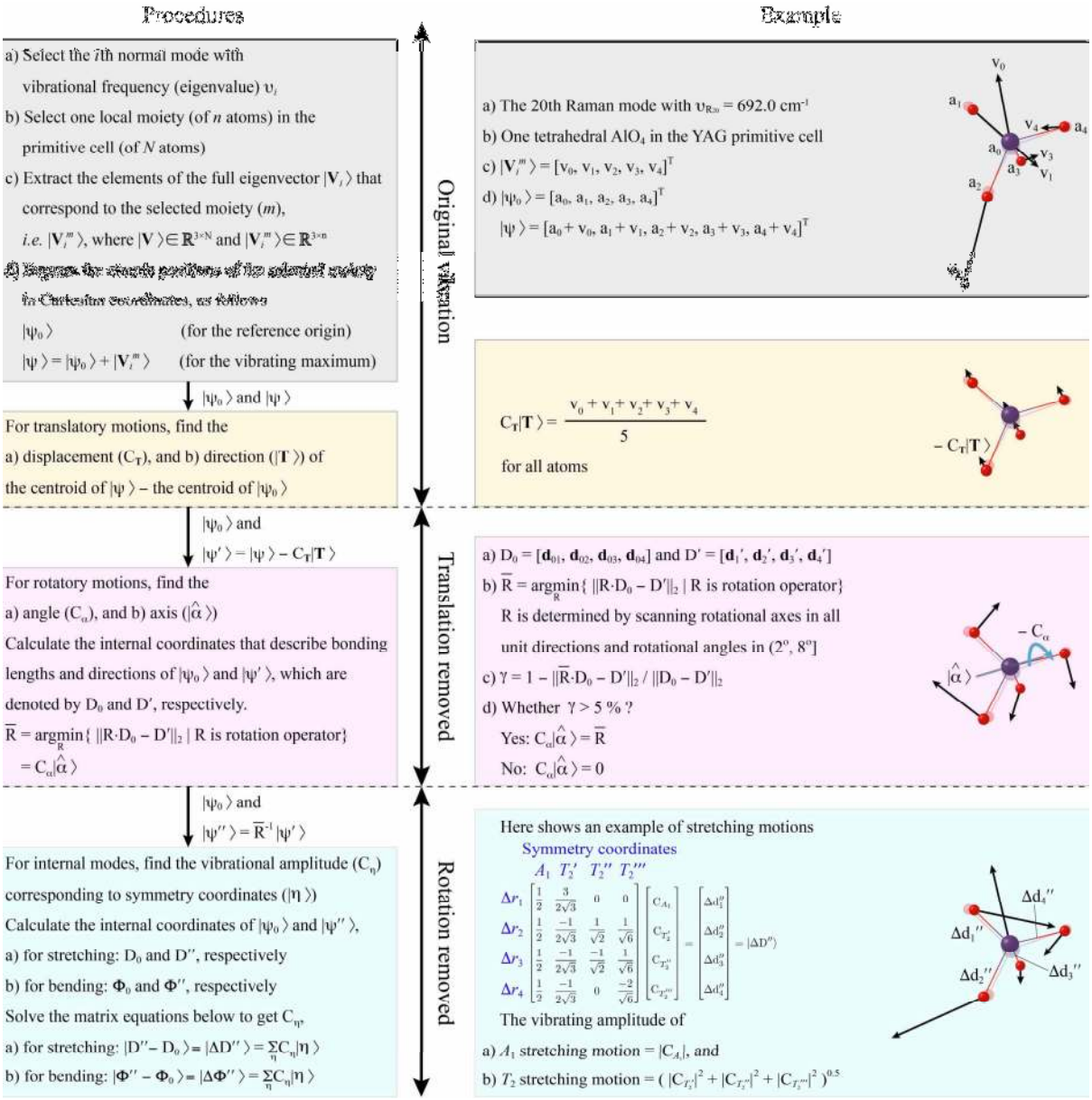

Figure 2: *Left:* flowchart describing the decomposition of extended lattice vibrational modes (phonons) into localized (molecular) vibrational modes. *Right:* An example, showing the extraction of the contribution from localized vibrations of one AlO_4 moiety to the 20th Raman mode at 692 cm^{-1}.

RESULTS

Vibrational Spectra of YAG and Phonon Assignment

The large number of atoms in the primitive cell leads to 240 (=3×80) possible normal modes, which can be classified according to the irreducible representation of the O_h^{10} group as follows:[8]

$$\begin{aligned}\Gamma = 5A_{1u} + 3A_{1g} + 5A_{2u} + 5A_{2g} + 10E_u + \\ 8E_g + 14T_{1g} + 18T_{1u} + 14T_{2g} + 16T_{2u}.\end{aligned} \quad (2)$$

Here, the A_{1g} modes are non-degenerate, the E_g modes are doubly degenerate, while the T_{1u} and T_{2g} are triply degenerate. The 25 modes having symmetries A_{1g}, E_g, and T_{2g} are Raman active, while the 18 modes having T_{1u} triply degenerate symmetry include (17 × 3) IR active modes and (1 × 3) acoustic modes.[8] In agreement with the group-theoretically predicted number of modes, there are 17 and 25 bands in the experimentally measured IR and Raman spectra, respectively (Figure 3). Vibrational frequencies determined by our *ab-initio* calculations [indicated as tick marks in Figure 3(a–b)] show an almost perfect agreement for all bands. Very good agreement is also obtained between the INS spectrum measured at 15 K and the calculated partial vibrational density of states (PDOS) weighted by the neutron scattering cross section [Figure 3(c)], which further confirms the high accuracy of the DFT calculations. A comparison between the INS spectrum and calculated PDOS show that the spectrum is dominated by the scattering from Y (100–250 cm^{-1}) and O (250–900 cm^{-1}) atoms, whereas Al vibrations are barely observable with INS due to the low neutron scattering cross section of this element (see above). It is also noted that the INS bands at approximately 99, 187, and 768 cm^{-1} are absent in the IR and Raman spectra and hence they are most likely related to optically inactive (silent) modes of YAG.

Figure 4 and S2 show the phonon decomposition maps (PDMs), *i.e.* the decomposition of the lattice phonon modes in terms of the localized vibrational modes of YO_8, AlO_4 and

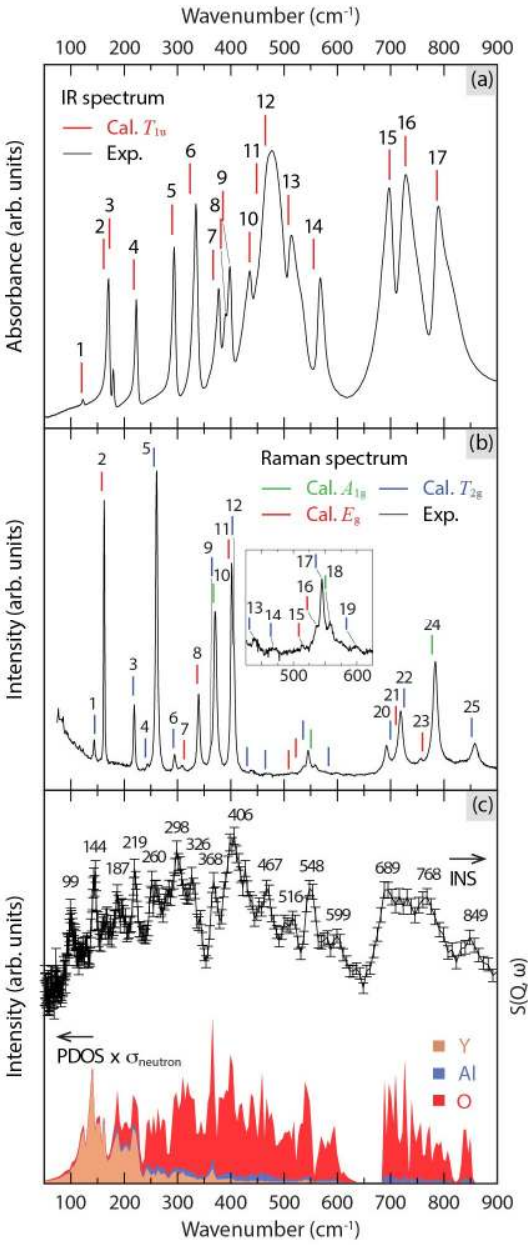

Figure 3: (a) IR and (b) Raman spectra of YAG. Tick marks show the calculated vibrational symmetry and frequency at the zone-center (Γ point). (c) Comparison of the INS spectrum of YAG measured at 15 K and calculated PDOS of YAG weighted by the total neutron scattering cross sections ($\sigma_{neutron}$) that are 7.7, 1.5 and 4.2 barns (1 barn = 1×10^{-24} cm^2) for Y, Al, and O atoms, respectively.

$AlO_6$for all Raman and IR-active as well as optically inactive (silent) phonon modes (left) together with the average atomic displacements of the YO_8, AlO_4 and AlO_6 moieties (right).

The vibrating amplitude of the local modes is plotted concentrically, which reveals the homogeneity of the same-type polyhedra in terms of vibrating amplitude. The homogeneity of the vibrating amplitudes amongst the same type of polyhedra (YO_8, AlO_6 or AlO_4) is reflected by the width of the the concentric bin. For example, the amplitude of the T_2 stretching motion of the AlO_4 moieties (I_{15}) is divided into one circle and one annulus of the same width but diff t color, which shall be interpreted as out of the total number of 12 AlO_4 moieties within the primitive cell, 6 of them vibrate with an amplitude of ≈55% (*cf.* color bar on top in Figure 4) compared to the maximum one, whereas the 6 remaining ones vibrate with an amplitude of ≈75%. In comparison, the homogeneous color of the mode I_{16} shall be interpreted as all the 12 AlO_4 moieties vibrate with the same amplitude (≈65%). Analysis of the PDMs yields the following insights: (i) in the low-frequency range (0–350 cm^{-1}), **S** motions due to strong Y displacements, as well as **T** and **R** motions of AlO_4 and AlO_6 units prevail (note that acoustic modes are not discussed here), (ii) in the medium-frequency range (350–600 cm^{-1}), **S** and **B** motions of YO_8, AlO_4 and AlO_6 moieties primarily involving O atoms dominate, and (iii) in the high-frequency range (600–900 cm^{-1}), **S** and **B** motions of AlO_4 and AlO_6 moieties involving both O and Al atoms, as well as **B** motions of YO_8 involving mostly O atoms are found. Generally, one observes with increasing vibrational frequency a systematic transition of YO_8 from **S** to **B** vibrations, and of AlO_6 and AlO_4 from external modes and **B** vibrations to **S** vibrations at higher frequencies.

Ce^{3+} Dopant Concentration Dependence

Figure 5 shows IR and Raman spectra for different Ce^{3+} dopant concentrations. The spectra display no abrupt changes with Ce^{3+} concentration, indicating the absence of phase transitions or significant structural degradations. In the low-frequency region (100–350 cm^{-1}), we observe a downward-shift of the bands located at 170 cm^{-1}, 222 cm^{-1}, 294 cm^{-1}, and 333 cm^{-1} in the IR spectrum, and at 143 cm^{-1}, 162 cm^{-1}, 218 cm^{-1}, 243 cm^{-1}, and 339 cm^{-1} in the Raman spectrum. The downward-shift depends virtually linearly on Ce^{3+} concentra-

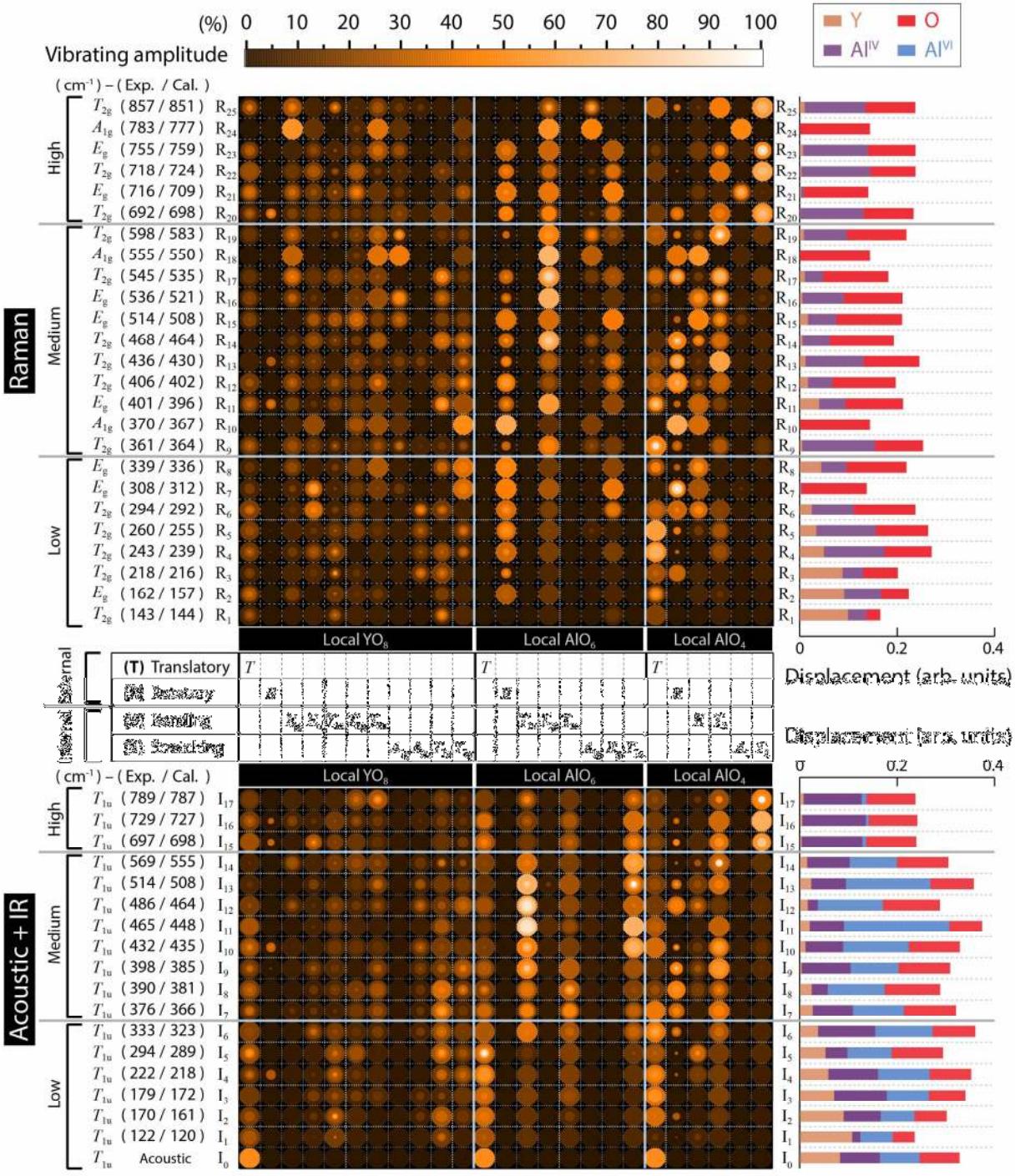

Figure 4: *Left:* full PDMs for Raman and IR-active normal modes of YAG. The vibrational amplitude is normalized to the maximum of the respective type (*i.e.* **T**, **R**, **B**, or **S**) of all 240 normal modes. For example, all **B** vibrations are normalized to the maximum of the T_{1u} **B** vibrations of the AlO_6 moieties that originate from the 35th silent mode (Si_{35}) in A_{2u} symmetry, see Figure S2. *Right:* averaged atomic displacements for Y, Al^{VI}, Al^{IV}, and O atoms.

tion (Figure S3) and is due to the larger mass of Ce^{3+} compared to that of Y^{3+}.[13,20,37] In the medium-frequency region (350–600 cm^{-1}), the positions of all bands are largely unaffected by Ce^{3+} concentration. In the high-frequency region (600–900 cm^{-1}), we observe a downward-shift (particularly for 3% Ce^{3+}) of the three highest-frequency bands in the IR spectrum at 697 cm^{-1}, 729 cm^{-1}, and 789 cm^{-1}, and of the six highest-frequency bands in the Raman spectrum at 692 cm^{-1}, 716 cm^{-1}, 718 cm^{-1}, 755 cm^{-1}, 783 cm^{-1}, and 857 cm^{-1}. Generally speaking, the number of vibrational bands is unchanged upon the Ce^{3+} substitution (of up to 3%) and, therefore, the vibrational (local) symmetries of YAG:Ce^{3+} can be interpreted as that of YAG (and thus the PDMs in Figure 4 and S2), as described above.

Temperature Dependence

Figure 6 shows Raman spectra recorded for YAG at temperatures from 80 to 870 K, and the IR spectra of YAG and YAG:3%Ce^{3+} for temperatures between 300 and 780 K; the variable temperature IR spectra of YAG:1%Ce^{3+} are shown in Figure S4. In agreement with the spectra for diff t Ce^{3+} doping levels (Figure 5), the spectra display no abrupt changes upon the temperature variation, confirming that no phase transitions or significant structural degradations are taking place. This is also reflected by the fact that no discontinuities in properties such as luminescence spectra and emission decay dynamics are observed within the probed temperature range.[38]

From the spectral changes, it is apparent that the peaks generally shift towards lower frequencies with increasing temperature. The downward-shift magnitude scales with the vibrational mode frequency, suggesting that it is predominantly the result of thermal lattice expansion whose effect on vibrational frequency has been calculated, as shown in Figure S5. The calculated frequency downward-shift is generally larger than the experimental one. This may be due to an overestimation of the thermal lattice expansion, which is common for the PBE functional.[39]

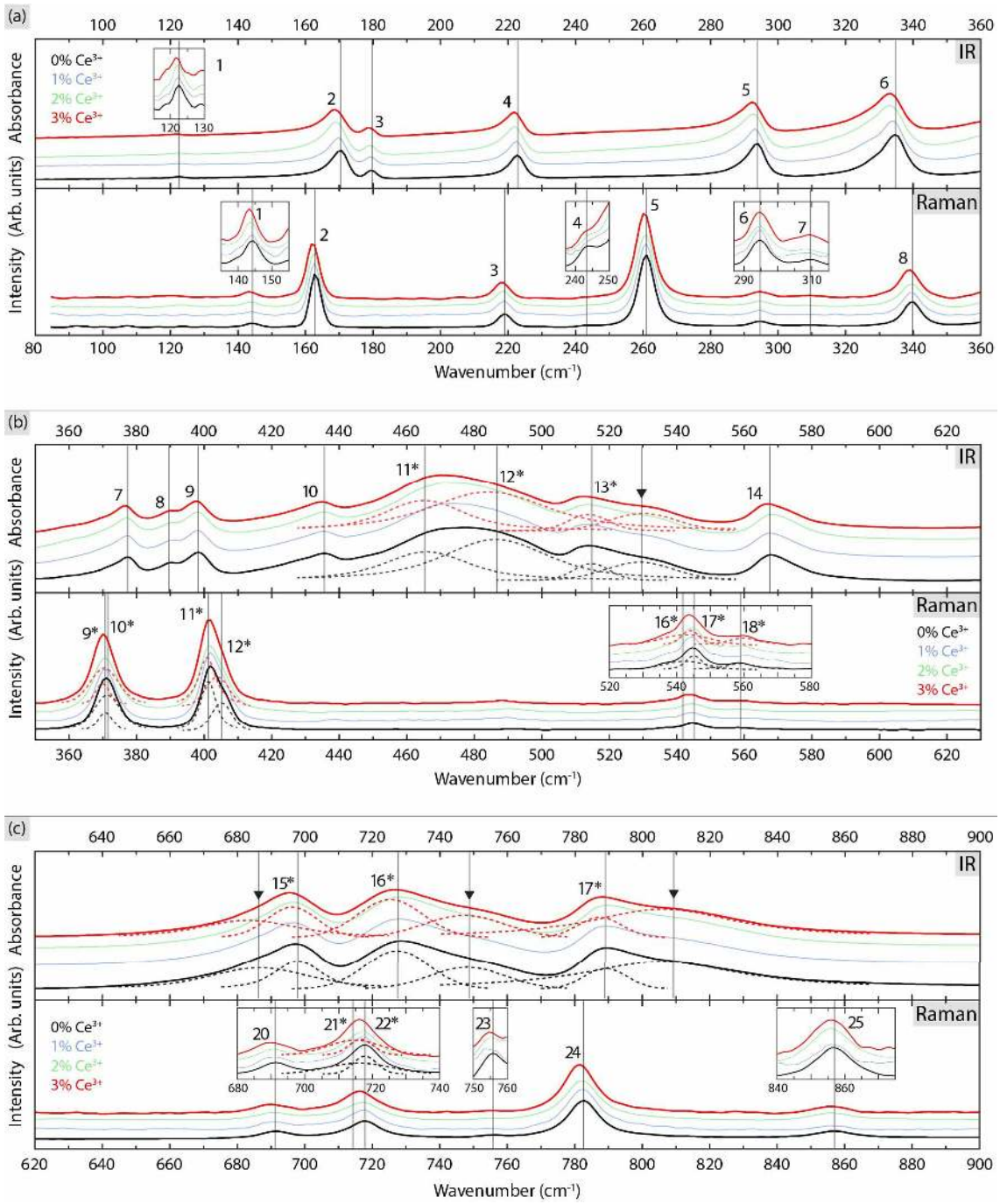

Figure 5: IR and Raman spectra of YAG :z%Ce^{3+} (z = 0, 1, 2, and 3), divided into frequency ranges of (a) 80–360 cm^{-1}, (b) 350–630 cm^{-1}, and (c) 620–900 cm^{-1}. Dashed curves are Voigt-function fits for overlapping bands, which are marked with asterisks (∗). Some unidentified bands in the IR spectra are marked by downward triangles (T). Vertical lines are positioned at the maxima of the IR and Raman bands of YAG.

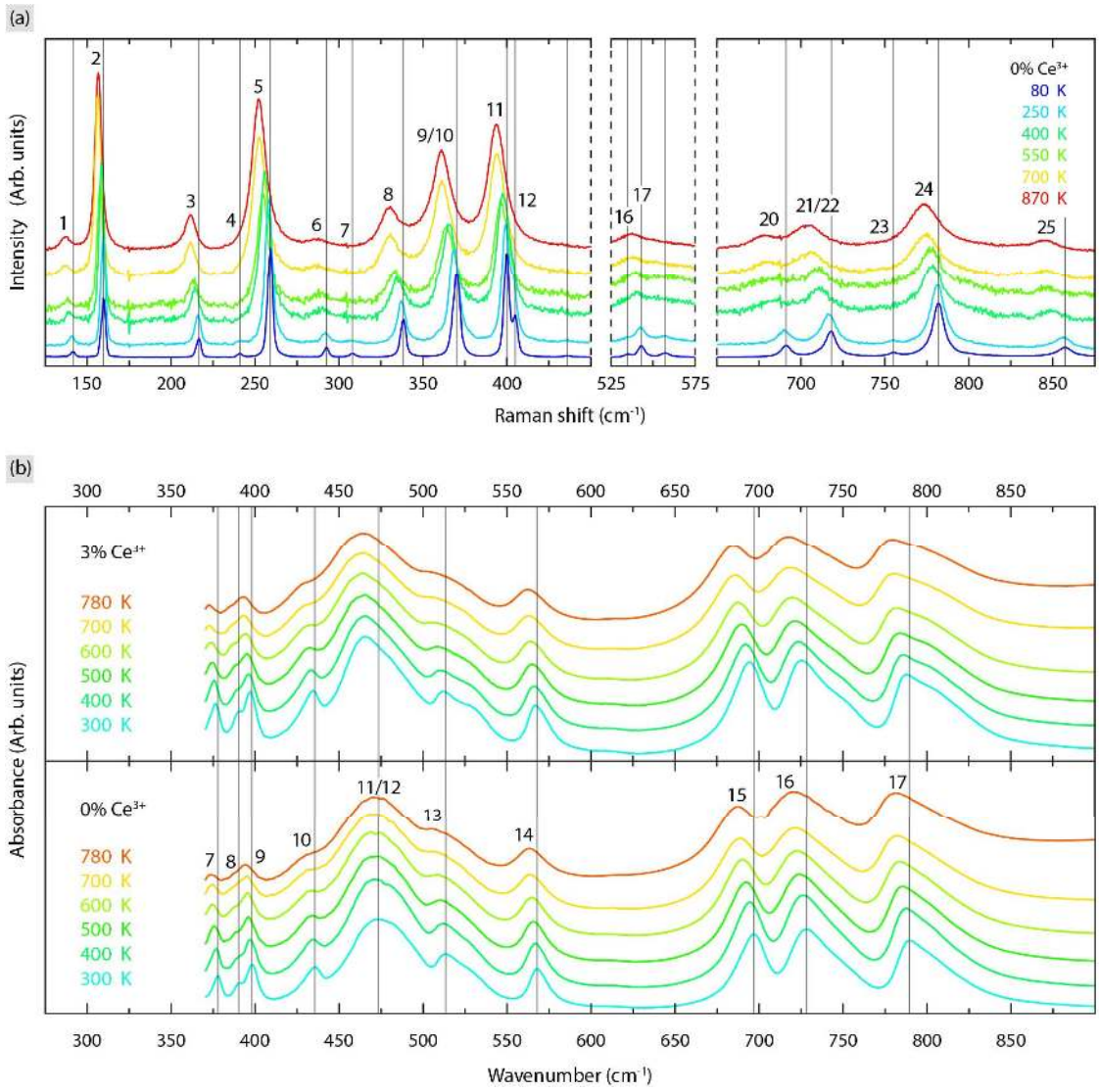

Figure 6: (a) Raman spectra of YAG between 80 and 870 K, and (b) IR spectra of YAG :z%Ce^{3+} (z = 0, and 3) from 300 to 780 K. Vertical lines are positioned at the maxima of the IR and Raman bands of YAG.

Photoluminescence Emission Spectra

The emission spectra of YAG:Ce^{3+}(Figure 7), as normalized to the emission band maxima, show that the peak positions are very similar for 1% and 2% Ce^{3+}, whereas a significant red-shift is observed for 3% Ce^{3+}. The peak fitting for the $^2F_{5/2}$ and $^2F_{7/2}$ bands shows a systematic spectral broadening with increasing Ce^{3+} concentration, as apparent from the full width at half maximum (FWHM) in Figure 7.

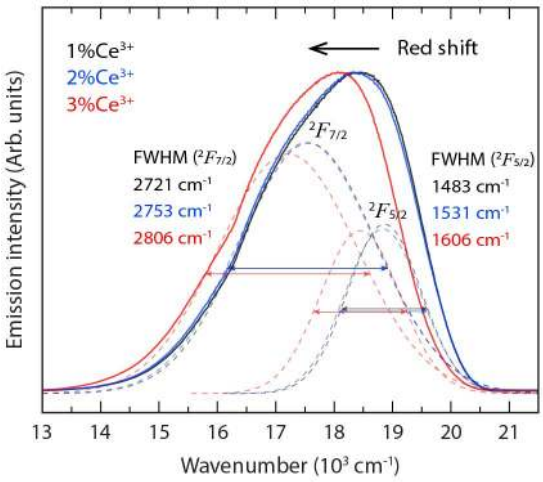

Figure 7: Emission spectra of YAG :z%Ce^{3+} (z = 1, 2, and 3), as normalized to the emission band maxima, at 300 K.

DISCUSSION

In the present study, we have combined vibrational spectroscopy and *ab-initio* calculations to provide a complete phonon assignment of YAG in terms of the vibrational dynamics of individual AlO_4 tetrahedra, AlO_6 octahedra, and YO_8 dodecahedra of the $Y_3Al_5O_{12}$ structure, and provide an assignment of all peaks in the experimental Raman and IR spectra for the first time. Analyses of the vibrational spectra establish general spectral trends, in particular frequency shifts, upon varying Ce^{3+} dopant concentration and temperature. To summarize our results, the Raman, IR, INS, and *ab-initio* calculations are in excellent agreement, demonstrating no abrupt changes with Ce^{3+} dopant level and temperature variations, meaning that the overall symmetry of the crystal structure of $Y_{3-x}Ce_xAl_5O_{12}$ is maintained for all Ce^{3+} dopant concentrations ($x = 0 - 0.09$) and temperatures ($T = 80 - 870$ K) investigated here.

From the observed spectral changes with increasing Ce^{3+} concentration, the downward-shift of peaks in the low-frequency region, < 350 cm^{-1}, together with the fact that these peaks are characterized by large-amplitude Ce/Y motions, suggests the downward-shift is related to the larger mass of Ce^{3+} (140 u) compared to Y^{3+} (89 u).[13,20,37] This is in agreement

with recent vibrational spectroscopy studies of aluminum garnets differing in the rare earth (RE) element, $RE_3Al_5O_{12}$ (RE = Lu, Tb, or Gd). This is illustrated in Figure 8, which shows the shift in vibrational frequency for (a) IR and (b) Raman-active modes for $RE_3Al_5O_{12}$ (RE = Lu, Tb, or Gd), as compiled from literature data,[15,40] in comparison to the peak positions for YAG determined in the present work. In line with our results, the frequency of the low-frequency modes (100–300 cm^{-1}) for $RE_3Al_5O_{12}$ (RE = Y, Lu, Tb, or Gd) exhibits a systematic relationship with increasing atomic weight of the RE cation, Y^{3+} (89 u) < Ce^{3+} (140 u) < Gd^{3+} (157 u) < Tb^{3+} (159 u) < Lu^{3+} (175 u).

In contrast to the low-frequency region, the downward-shift of peaks in the high-frequency range (600–900 cm^{-1}) shows no such a mass effect (Figure 8); rather, we observe a dependence on the ionic radius of the RE ion. The ionic radii of the respective RE ions are 1.12 Å for Lu^{3+}, 1.16 Å for Y^{3+}, 1.18 Å for Tb^{3+}, 1.19 Å for Gd^{3+}, and 1.28 Å for Ce^{3+} in eight-fold coordination.[41] The fact that the vibrational frequency is higher for RE ions with smaller ionic radii is consistent with shorter and stronger RE-O bonds, and *vice versa*. We note, however, that these high-frequency vibrational modes are primarily dominated by large-amplitude internal-mode motions of the AlO_4 and AlO_6 moieties, suggesting that the effect of the size of the RE ion is not limited to their immediate environment. As the REO_8 moieties share edges with both AlO_4 and AlO_6 units in the garnet structure, it is not surprising that some changes in the dynamics of the AlO_4 and AlO_6 moieties occur to accommodate a RE ion with a different size. Changes in the vibrational frequency of these high-frequency modes may be due to changes in either the average Al–O distances or in the local structural symmetry of the AlO_4 and AlO_6 moieties, or both. The latter is supported by the results by Arvanitidis *et al.*,[13] who observed a pressure-induced blue-shift of the high-frequency modes of YAG, as a result of increased distortion of the AlO_4 and AlO_6 moieties as a way to accommodate for a decreasing unit-cell volume.

Since the vibrational dynamics is known to infl the macroscopic optical properties of YAG:Ce^{3+}, the insights gained here are important for developing an improved under-

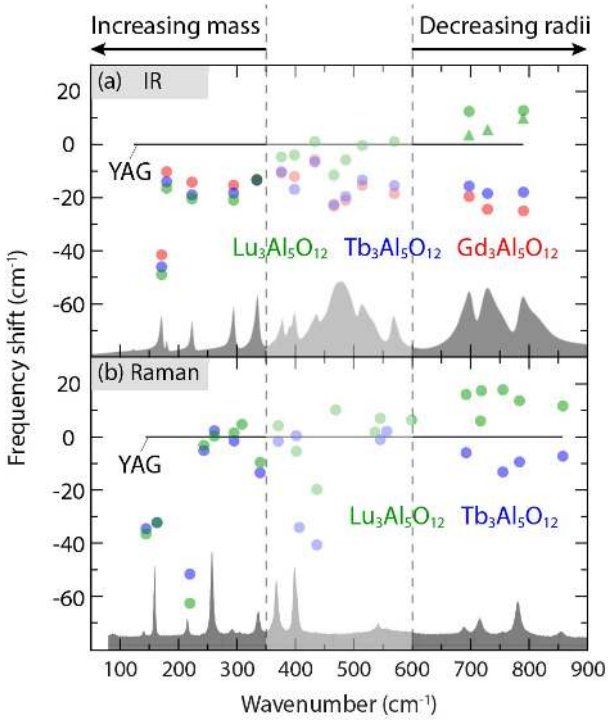

Figure 8: Vibrational frequency shifts of (a) IR and (b) Raman modes of aluminum garnets ($RE_3Al_5O_{12}$, RE: rare-earth element) when RE (= Y) is completely substituted by Lu, Tb or Gd. The vibrational frequencies of $RE_3Al_5O_{12}$ are taken from the measured spectra of YAG [Figure 3(a–b)], ref. 15 and ref. 40, whose frequency shifts are marked by black lines, circles and triangles, respectively.

standing of the origins of the luminescent performance of YAG:Ce^{3+}. A key characteristic when comparing the emission spectra of YAG:1%Ce^{3+}, YAG:2%Ce^{3+}, and YAG:3%Ce^{3+}, as studied here, is the significantly red-shifted spectrum for YAG:3%Ce^{3+}, *cf.* Figure 7 and ref. 38. In this context, we note that the red-shift of the emission spectrum for YAG:3%Ce^{3+} correlates with the observed downward-shift of some of the high-frequency vibrational modes for this material [Figure 5(c)], which may therefore be attributed to a significant modification of local vibrational dynamics around the Ce^{3+} ions. By contrast, for the two lower Ce^{3+} dopant concentrations, the spectra are not significantly different from that of the undoped compound (YAG). The similar emission and vibrational spectra for YAG:1%Ce^{3+} and YAG:2%Ce^{3+} suggest no significant differences in the local coordination of the Ce^{3+} dopants for these dopant concentrations. In comparison, the red-shift for YAG:3%Ce^{3+} suggests that

the higher Ce^{3+} dopant level leads to a lowering of the Ce^{3+} $5d_1$ level (increased Stokes shift) as an effect of increased crystal-field splitting due to Ce^{3+}-induced local structural distortions. Seijo *et al.*[42] investigated the effect of distortions of the Ce^{3+} coordination shell on its $4f$ and $5d$ electronic configurations with embedded-cluster wave-function based *ab-initio* methods. The only deformations of a CeO_8 moiety that were found to lower the $5d_1$ level are the symmetric Ce–O bond compression and the tetragonally symmetric bond bending, which have been assigned to the A_{1g} and E_g symmetries of the O_h irreducible symmetry group (*e.g.* cubic CeO_8), respectively. The observed red-shift of the emitted light with increasing Ce^{3+} dopant level may thus be linked to an increased degree of tetragonal distortion of the CeO_8 dodecahedra as the relatively large Ce^{3+} ions substitute for the smaller Y^{3+} ions. The strengthening of the tetragonal distortion of the CeO_8 dodecahedra with increasing Ce^{3+} concentration is in agreement with the magnitude of the lattice expansion with Ce^{3+} doping, which is smaller (more compressed and distorted local environment) than expected.[11] Given a random distribution of the Ce^{3+} dopants, it is clear that the effect of tetragonal distortions will not be limited to the immediate neighborhood of the dopant atom. Rather the effect of an increase of the tetragonal distortion of the CeO_8 dodecahedra is expected to distribute throughout the lattice already at a quite low dopant level. On the basis of the observed vibrational spectra (Figure 5) and emission spectra (Figure 7), a "compositional threshold" for the distribution of the effect of the increase of the tetragonal distortions of individual, "uncorrelated", CeO_8 dodecahedra throughout the garnet lattice may possibly be located between $x = 0.06$ and $x = 0.09$.

Another plausible explanation for the observed red-shift upon increasing Ce^{3+} concentration is an increase in the degree of dynamical tetragonal distortions of the CeO_8 moieties through the increment of large-amplitude CeO_8 E_g **B** vibrations, *e.g.* $R_{24}(A_{1g})$ and $R_{25}(T_{2g})$, *cf.* Figure 4. This is supported by the downward-shift of these vibrational modes as a function of Ce^{3+}, since more phonons with lower frequencies are activated. Such an effect could also explain the systematic red-shift of the emission peak as a function of increasing size of

the RE ion in $RE_3Al_5O_{12}:Ce^{3+}$ (RE = Gd, Tb, Y or Lu), see the corresponding emission maxima in refs. 43–45, due to the lowering of the vibrational frequency of high-frequency modes (Figure 8). Additionally, the red-shifted emission may originate from an increased probability of radiative energy transfer from higher to lower $5d_1$ levels between Ce^{3+} ions, through re-absorption processes that depends on the degree of spectral overlap between the excitation and emission spectra.[11,38,46] In fact, Figure 7 shows an increasing FWHM of the $5d$–$4f$ emission band as a function of Ce^{3+} concentration, which supports this view.

Table 1: Excitation maximum, λ_{ex},[a,b] emission maximum, λ_{em} (Figure 7), Stokes shift, ΔS,[c] and thermal quenching temperature, $T_{80\%}$,[d] of $YAG:Ce^{3+}$.

$YAG:Ce^{3+}$	λ_{ex} (nm)	λ_{em} (nm)	ΔS (cm^{-1})	$T_{80\%}$ (K)
1% Ce^{3+}	460 [a]	541	2900	645
2% Ce^{3+}	460 [b]	544	2900	–
3% Ce^{3+}	460 [a]	553	3300	580

[a] Estimated from luminescence excitation spectra in ref. 38.

[b] Estimated from luminescence excitation spectra in ref. 11.

[c] Estimated from the difference between λ_{ex} and the maximum of the $^2F_{5/2}$ emission band in Figure 7. The here determined ΔS is larger than that reported in the literature[38] for YAG:0.033%Ce^{3+} (ΔS = 2400 cm^{-1}), which may be ascribed to the lower Ce^{3+} concentration and measuring temperature (5 K) in the previous study[38] compared to our one.

[d] $T_{80\%}$ refers to the temperature at which the luminescence lifetime has dropped to 80% of the value at 300 K. It has been estimated from the temperature dependence of the luminescence decay time, as reported in ref. 38.

Besides the red-shift, the substitution of Ce^{3+} ions for Y^{3+} also has important implications with regard to thermal quenching in $YAG:Ce^{3+}$, which refers to the pronounced reduction in emission intensity observed at elevated temperatures. On a fundamental level, the three primary processes that are thought to play a role in the thermal quenching of luminescence in Ce^{3+}-doped materials exhibiting $5d$–$4f$ luminescence are (1) thermal ionization of the Ce^{3+} $5d$ electrons into the conduction band of the host crystal, followed by charge trapping [Figure 9(a)],[47,48] (2) thermally-activated non-radiative energy migration among Ce^{3+} ions to killer centres (generally known as concentration quenching[38,46]), see Figure 9(b),

and (3) thermally activated crossover from the 5*d* excited state to the 4*f* ground state *via* electron-phonon coupling mechanisms [Figure 9(c)]. Regardless of the mechanism(s) (their respective contribution(s) are not known), phonons are needed to bring the excited activator ion to a point at which non-radiative processes can happen. Although the nature of phonons involved in thermal quenching mechanisms remains unclear, analyses of high-resolution low-temperature luminescence spectra of YAG:Ce^{3+} have revealed a vibronic fine structure with features (phonon replicas) at around 200 cm^{-1} relative to the zero-phonon line,[38,49] which has been interpreted as evidence for electron-phonon interactions involving a vibrational mode at this frequency. YAG features modes at 218 (R_3), 179 (I_3), 222 (I_4), 184 (S_6), and 214 (S_7), 217 cm^{-1}(S_8), see Figure 4 and S2, which are quite close in frequency to the observed 200 cm^{-1} ~~feature~~ phonon replicas. Apart from these modes, a few weak phonon replicas are observed also in the frequency range of 130–160 cm^{-1} at sufficiently low temperature (4 K),[49] which may be associated with the phonon modes of YAG at 143 (R_1), 162 (R_2), 122 (I_1), 170 (I_2), 132 (S_1), 141 (S_2), 148 (S_3), 166 (S_4), and 171 cm^{-1}(S_5). The less pronounced features below 200 cm^{-1} may indicate weaker electron-phonon coupling, and/or the smearing out of these features as a result of the thermal excitation of these phonon modes that require less energy as compared to those at around 200 cm^{-1}. The trend of decreasing vibrational frequency for some of these modes (*i.e.* R_1, R_2, R_3, I_2, and I_4) as a function of increasing Ce^{3+} concentration would suggest a larger population of these modes at a given temperature and hence also an increased probability of electron-phonon interactions that may be associated with $5d_1 \rightarrow 4f$ crossover non-radiative relaxation and that lead to a lowering of $T_{80\%}$ (Table 1). Yet the simultaneous downward-shift of modes in the higher frequency range, 600–900 cm^{-1}, with increasing Ce^{3+} concentration may indicate that these modes are important for thermal quenching as well. The relevance of high-frequency phonons in electron-phonon interactions is in accordance with recent studies of the similar material $Y_{3-x}Lu_xAl_5O_{12}:Ce^{3+}$, which, compatible with the observations for YAG:Ce^{3+}, shows a trend of increasing temperature of thermal quenching with increasing frequency of vibrational modes in the 600–900 cm^{-1} range

(*cf.* $T_{50\%}$ > 700 K for YAG:Ce^{3+} and $T_{50\%}$ > 800 K for $Lu_3Al_5O_{12}$:Ce^{3+}, where $T_{50\%}$ refers to the temperature at which the quantum efficiency (QE) has dropped to 50% of that at low temperature[45]). The upward-shift of modes for LuAG:Ce^{3+} compared to YAG:Ce^{3+} is also reflected in the higher structural rigidity of LuAG:Ce^{3+}, which is likely to be the reason for its higher QE and higher luminescence thermal stability,[6,44,45,50,51] *i.e.* less pronounced phonon-induced non-radiative relaxation. Further support for significant electron-phonon coupling mechanisms contributing to the observed thermal quenching of YAG:Ce^{3+} and LuAG:Ce^{3+} comes from the fact that the quenching temperature of LuAG:Ce^{3+} is ≈100 K higher than that of YAG:Ce^{3+}, and the energy gaps between the conduction band minimum and Ce^{3+} $5d_1$ level in these materials are very similar (*cf.* 1.07 eV for YAG:Ce^{3+} and 1.05 eV for LuAG:Ce^{3+}).[52] If thermal ionization would namely be the dominating process, one would expect to observe a similar thermal quenching temperature in these two materials. A similar effect of Y/Lu substitution on thermal quenching is also observed for another Ce^{3+}-doped oxide phosphor, $Ba_2(Y_{1-x}Lu_x)_5B_5O_{17}$:$Ce^{3+}$.[53] Further, an increase in luminescence thermal stability with increasing vibrational frequency of modes (which correlate with smaller RE atoms) is also observed for $RE_3Al_5O_{12}$:Ce^{3+} (RE = Y, Tb, or Gd),[43] (Figure 8), although it should be noted that the predominant mechanism for thermal quenching may be different in the different materials.

The correlation between an upward-shift of vibrational modes, increased structural rigidity, quenching temperature, and QE in YAG:Ce^{3+} is in agreement with the predictions by George *et al.*[11] Specifically, the combined analyses of the vibrational dynamics and luminescence properties of YAG:Ce^{3+} in this work suggest that the apparent decrease in quenching temperature (Table 1) and QE with increasing Ce^{3+} concentration results from the substitution of Y^{3+} for the heavier Ce^{3+} ions and Ce^{3+}-induced increased local structural disorder, both of which lead to a lowering of vibrational frequencies and thus a softening of the material. In this context, we note that the Debye temperature of YAG:Ce^{3+}, which provides a useful estimate for structural rigidity, decreases by >200 K as the Ce^{3+} concentration increases

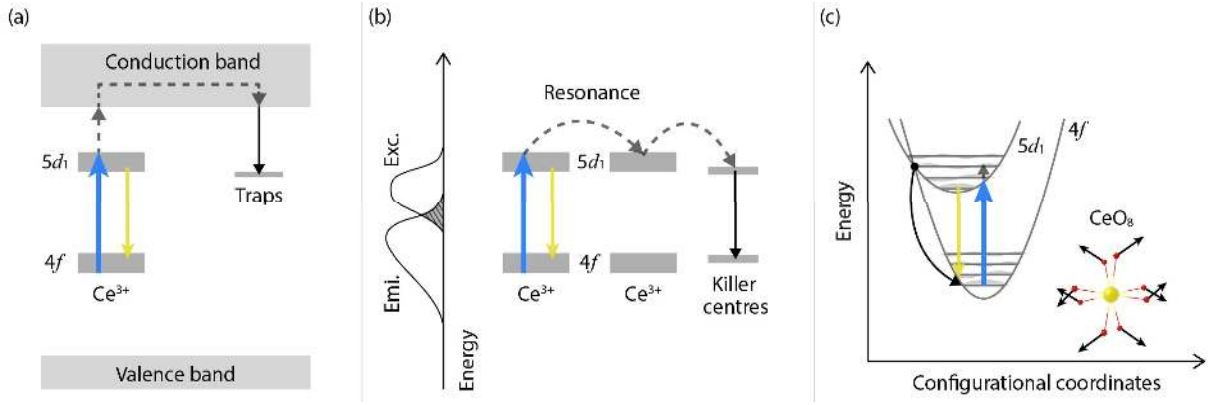

Figure 9: Schematic illustration of (a) thermal ionization of the Ce^{3+} 5*d* electrons into the conduction band of the host crystal followed by charge trapping at defect levels, (b) thermally-activated concentration quenching by non-radiative energy migration among Ce^{3+} ions to killer centres (the overlap between the excitation (Exc.) and emission (Emi.) spectra is indicated to the left, and the overlap integral determines the probability of resonance transfer of excitation energy[46]), and (c) thermally activated crossover from the 5*d* excited state to the 4*f* ground state *via* electron-phonon coupling. The schematic to the lower right in (c) depicts the local vibrations of CeO_8, with a frequency of 783 cm^{-1}, as extracted from the $R_{24}(A_{1g})$ mode in Figure 4.

from 0 to 3%.[11] In comparison, the isotropic thermal lattice expansion from T = 300 K to T = 1200 K reduces the Debye temperature by a relatively much smaller amount (Table S2). Thus, we infer that the effect of increased phonon population due to thermal lattice expansion on the thermal quenching temperature of YAG:Ce^{3+} is smaller than the effect of local structural modifi due to Ce^{3+} doping.

The enhancement of electron-phonon coupling mechanisms with increasing Ce^{3+} concentration is in agreement with a broadening of the Ce^{3+} 4*f*–5*d* excitation (see the spectrum in ref. 38) and emission bands (Figure 7) as a function of increasing Ce^{3+} concentration. Broadening may, however, also be a signature of an increasing energy distribution of the Ce^{3+} 5*d* levels due to increased local structural distortions that make the Ce^{3+} 4*f*–5*d* transition energy less defined. In this context, we note that the excitation and emission spectra of YAG:Ce^{3+} show a larger Stokes shift, ΔS, for higher Ce^{3+} dopant levels (ref. 38 and Table 1). The increased Stokes shift reflects an increased difference of the equilibrated Ce–

O distance between 4*f* ground state and 5d_1 excited state of Ce^{3+}, and maybe in turn be associated with the enhanced tetragonal distortion of CeO_8, which shortens the equilibrium Ce–O distance when the 4*f* electron is excited into the 5*d* orbital. The increased Stokes shift is thereby associated with stronger electron-phonon interactions, which is in agreement with the broadening of the emission spectra shown in Figure 7 and in ref. 38. The broadening of the luminescence spectra as a function of Ce^{3+} concentration is in agreement with the observed downward-shift of most vibrational modes of the Ce^{3+} ions, as the lowering in vibrational frequency implies a smaller curvature of both the 4*f* and 5*d* parabolae in the configurational coordinate diagram[54,55] Also, widening of the parabolae narrows the distribution between vibrational states within the parabolae, meaning they become more easily populated at a given temperature. This is of particular importance for the activation of vibrational induced tetragonal distortions of the CeO_8 moieties, as discussed above.

By bringing together the results from our combined vibrational and luminescence spectroscopy study we find that a softening of the crystal lattice due to increasing Ce^{3+} concentration or temperature leads to a downward-shift of phonon modes at frequencies higher than about 600 cm^{-1}, which are mainly related to CeO_8 bending modes. This causes a red-shift of the emitted light, which is interpreted as an increase of the crystal-field splitting due to an increased tetragonal distortion of the CeO_8 moieties. In comparison, an increased structural rigidity, through decreasing Ce^{3+} concentration or by the co-substitution of smaller and/or lighter atoms for the Y atoms of the YAG host lattice, shows the potential to improve the resistance toward thermal quenching of luminescence, since fewer phonon modes are activated that are important for non-radiative relaxation mechanisms. A scenario thus emerges in which the development of new phosphors emitting at longer wavelengths requires tetragonally distorted environments around the CeO_8 moieties, combined with a rigid host structure and low activator-ion concentrations to avoid thermal quenching of luminescence.

CONCLUSIONS

We provide a complete phonon assignment of YAG in terms of the vibrational dynamics of individual AlO_4 tetrahedra, AlO_6 octahedra, and YO_8 dodecahedra of the $Y_3Al_5O_{12}$ structure, and assign all the peaks in the experimental Raman, IR and INS spectra. Analysis of the vibrational spectra establish general spectral trends, in particular frequency shifts, with Ce^{3+} dopant concentration ($x = 0 - 0.09$) and temperature ($T = 80 - 870$ K), which are shown to correlate with the macroscopic optical properties of $Y_{3-x}Ce_xAl_5O_{12}$. The vibrational spectra demonstrate no abrupt changes with Ce^{3+} concentration and temperature, suggesting that the overall symmetry of the crystal structure of $Y_{3-x}Ce_xAl_5O_{12}$ is the same for all Ce^{3+} dopant levels and temperatures, in agreement with photoluminescence and luminescence lifetime measurements reported in the literature. Softening of the crystal lattice with increasing Ce^{3+} concentration or temperature leads to a downward-shift of phonon modes at frequencies higher than about 600 cm^{-1}, which are mainly related to CeO_8 bending modes. This causes a red-shift of the emission maximum, which we attribute to a larger crystal-field splitting as the result of an increased tetragonal distortion of the CeO_8 moieties. Increased structural rigidity, either due to a decreasing Ce^{3+} concentration or the substitution of smaller and/or lighter atoms for Y atoms, indicates the potential to improve the resistance toward thermal quenching of luminescence by activating fewer phonon modes of importance for non-radiative relaxation mechanisms. Effective design rules for finding new Ce^{3+} doped oxide phosphors inferred from these results establish that new phosphors emitting at longer wavelengths require tetragonally distorted environments around the CeO_8 moieties, and that a sufficiently rigid host structure and/or low activator-ion concentration is needed to avoid thermal quenching of luminescence.

ASSOCIATED CONTENT

Supporting Information Available

This material is available free of charge via the Internet at http://pubs.acs.org/.

- Illustration of all symmetry coordinates of cubic, octahedral, and tetrahedral moieties; full phonon decomposition map for the silent modes of YAG; vibrational frequency shift of YAG:Ce^{3+} upon increasing Ce^{3+} dopant concentration; temperature dependent IR spectra of YAG :z%Ce^{3+}; vibrational frequency shift of YAG upon increasing temperature (PDF)

AUTHOR INFORMATION

Corresponding Author

*E-mail: maths.karlsson@chalmers.se

ORCID

Yuan-Chih Lin: 0000-0002-0028-7481

Paul Erhart: 0000-0002-2516-6061

Marco Bettinelli: 0000-0002-1271-4241

Stewart F. Parker: 0000-0002-3228-2570

Maths Karlsson: 0000-0002-2914-6332

Notes

The authors declare no competing financial interests.

Acknowledgement

This research was funded primarily by the Swedish Research Council (grant No. 2010-3519), the Swedish Graduate School in Materials Science, the Swedish Foundation for Strategic Research (grant No. ICAIO-0001), and the Knut and Alice Wallenberg foundation. N.C.G. has been supported by the ConvEne IGERT Program of the U.S. NSF (NSF-DGE 0801627). The research made use of the Central Facilities of the UCSB Materials Research Laboratory, supported by the MRSEC Program of the NSF under Award DMR-1121053, which is a member of the NSF-funded Materials Research Facilities Network (www.mrfn.org). We also gratefully acknowledge the STFC Rutherford Appleton Laboratory for access to neutron beam facilities as well as computer time allocations by the Swedish National Infrastructure for Computing at NSC (Linköping) and PDC (Stockholm).

References

(1) Lin, Y.-C.; Karlsson, M.; Bettinelli, M. Inorganic Phosphor Materials for Lighting. *Top. Curr. Chem.* **2016**, *374*, 21.

(2) Qin, X.; Liu, X.; Huang, W.; Bettinelli, M.; Liu, X. Lanthanide-Activated Phosphors Based on 4*f*-5*d* Optical Transitions: Theoretical and Experimental Aspects. *Chem. Rev.* **2017**, *117*, 4488–4527.

(3) Lin, C. C.; Liu, R.-S. Advances in Phosphors for Light-Emitting Diodes. *J. Phys. Chem. Lett.* **2011**, *2*, 1268–1277.

(4) Xia, Z.; Meijerink, A. Ce^{3+}-Doped garnet phosphors: composition modification, luminescence properties and applications. *Chem. Soc. Rev.* **2017**, *46*, 275–299.

(5) Atuchin, V. V.; Beisel, N. F.; Galashov, E. N.; Mandrik, E. M.; Molokeev, M. S.; Yelisseyev, A. P.; Yusuf, A. A.; Xia, Z. Pressure-Stimulated Synthesis and Lumines-

cence Properties of Microcrystalline $(Lu,Y)_3Al_5O_{12}:Ce^{3+}$ Garnet Phosphors. *ACS Appl. Mater. Interfaces* **2015**, *7*, 26235–26243.

(6) Ji, H.; Wang, L.; Molokeev, M. S.; Hirosaki, N.; Xie, R.; Huang, Z.; Xia, Z.; ten Kate, O. M.; Liu, L.; Atuchin, V. V. Structure Evolution and Photoluminescence of $Lu_3(Al,Mg)_2(Al,Si)_3O_{12}:Ce^{3+}$ Phosphors: New Yellow-Color Converters for Blue LED-Driven Solid State Lighting. *J. Mater. Chem. C* **2016**, *4*, 6855–6863.

(7) Geller, S. Crystal Chemistry of the Garnets. *Z. Kristallogr. Cryst. Mater.* **1967**, *125*, 1–47.

(8) Hurrell, J. P.; Porto, S. P. S.; Chang, I. F.; Mitra, S. S.; Bauman, R. P. Optical Phonons of Yttrium Aluminum Garnet. *Phys. Rev.* **1968**, *173*, 851–856.

(9) Wu, J. L.; Gundiah, G.; Cheetham, A. K. Structure-Property Correlations in Ce-Doped Garnet Phosphors for Use in Solid State Lighting. *Chem. Phys. Lett.* **2007**, *441*, 250–254.

(10) Kalaji, A.; Saines, P. J.; George, N. C.; Cheetham, A. K. Photoluminescence of Cerium-Doped $(Ca_{1-x}Sr_x)_3RE_2Ge_3O_{12}$ Garnet Phosphors for Solid State Lighting: Relating Structure to Emission. *Chem. Phys. Lett.* **2013**, *586*, 91–96.

(11) George, N. C.; Pell, A. J.; Dantelle, G.; Page, K.; Llobet, A.; Balasubramanian, M.; Pintacuda, G.; Chmelka, B. F.; Seshadri, R. Local Environments of Dilute Activator Ions in the Solid-State Lighting Phosphor $Y_{3-x}Ce_xAl_5O_{12}$. *Chem. Mater.* **2013**, *25*, 3979–3995.

(12) Pan, Y.; Wu, M.; Su, Q. Tailored Photoluminescence of YAG:Ce Phosphor through Various Methods. *J. Phys. Chem. Solids* **2004**, *65*, 845–850.

(13) Arvanitidis, J.; Papagelis, K.; Christofilos, D.; Kimura, H.; Kourouklis, G. A.; Ves, S. High Pressure Raman Study of $Y_3Al_5O_{12}$. *Phys. Status Solidi B* **2004**, *241*, 3149–3154.

(14) Papagelis, K.; Arvanitidis, J.; Kanellis, G.; Kourouklis, G. A.; Ves, S. High Pressure Raman Study of $Lu_3Al_5O_{12}$. *Phys. Status Solidi B* **1999**, *211*, 301–307.

(15) Papagelis, K.; Ves, S. Infrared Spectroscopy and Lattice Dynamical Calculations of $Gd_3Al_5O_{12}$, $Tb_3Al_5O_{12}$ and $Lu_3Al_5O_{12}$ Single Crystals. *J. Phys. Chem. Solids* **2003**, *64*, 599–605.

(16) Papagelis, K.; Ves, S. Vibrational Properties of the Rare Earth Aluminum Garnets. *J. Appl. Phys.* **2003**, *94*, 6491–6498.

(17) Papagelis, K.; Arvanitidis, J.; Vinga, E.; Christofilos, D.; Kourouklis, G. A.; Kimura, H.; Ves, S. Vibrational Properties of $(Gd_{1-x}Y_x)_3Ga_5O_{12}$ Solid Solutions. *J. Appl. Phys.* **2010**, *107*, 113504.

(18) Moore, R. K.; White, W. B.; Long, T. V. Vibrational Spectra of the Common Silicates: I. The Garnets. *Am. Mineral.* **1971**, *56*, 54.

(19) Monteseguro, V.; Rodríguez-Hernández, P.; Vilaplana, R.; Manjón, F. J.; Venkatramu, V.; Errandonea, D.; Lavín, V.; Muñoz, A. Lattice Dynamics Study of Nanocrystalline Yttrium Gallium Garnet at High Pressure. *J. Phys. Chem. C* **2014**, *118*, 13177–13185.

(20) Papagelis, K.; Kanellis, G.; Ves, S.; Kourouklis, G. A. Lattice Dynamical Properties of the Rare Earth Aluminum Garnets ($RE_3Al_5O_{12}$). *Phys. Status Solidi B* **2002**, *233*, 134–150.

(21) Li, S.; Funahashi, R.; Matsubara, I.; Ueno, K.; Sodeoka, S.; Yamada, H. Synthesis and Thermoelectric Properties of the New Oxide Materials $Ca_{3-x}Bi_xCo_4O_{9+\delta}$ ($0.0 < x < 0.75$). *Chem. Mater.* **2000**, *12*, 2424–2427.

(22) Ju, L.; Sabergharesou, T.; Stamplecoskie, K. G.; Hegde, M.; Wang, T.; Combe, N. A.; Wu, H.; Radovanovic, P. V. Interplay between Size, Composition, and Phase Transition

of Nanocrystalline Cr^{3+}-Doped $BaTiO_3$ as a Path to Multiferroism in Perovskite-Type Oxides. *J. Am. Chem. Soc.* **2012**, *134*, 1136–1146.

(23) Yamazaki, Y.; Blanc, F.; Okuyama, Y.; Buannic, L.; Lucio-Vega, J. C.; Grey, C. P.; Haile, S. M. Proton trapping in yttrium-doped barium zirconate. *Nat. Mater.* **2013**, *12*, 647–651.

(24) Pathak, S. K.; Abate, A.; Ruckdeschel, P.; Roose, B.; Gödel, K. C.; Vaynzof, Y.; Santhala, A.; Watanabe, S.-I.; Hollman, D. J.; Noel, N.; Sepe, A.; Wiesner, U.; Friend, R.; Snaith, H. J.; Steiner, U. Performance and Stability Enhancement of Dye-Sensitized and Perovskite Solar Cells by Al Doping of TiO_2. *Adv. Funct. Mater.* **2014**, *24*, 6046–6055.

(25) Parker, S. F.; Fernandez-Alonso, F.; Ramirez-Cuesta, A. J.; Tomkinson, J.; Rudic, S.; Pinna, R. S.; Gorini, G.; Castañon, J. F. Recent and Future Developments on TOSCA at ISIS. *J. Phys. Conf. Ser.* **2014**, *554*, 012003.

(26) Blöchl, P. E. Projector Augmented-Wave Method. *Phys. Rev. B* **1994**, *50*, 17953–17979.

(27) Kresse, G.; Joubert, D. From Ultrasoft Pseudopotentials to the Projector Augmented-Wave Method. *Phys. Rev. B* **1999**, *59*, 1758–1775.

(28) Kresse, G.; Hafner, J. Ab Initio Molecular Dynamics for Liquid Metals. *Phys. Rev. B* **1993**, *47*, 558–561.

(29) Kresse, G.; Furthmüller, J. Efficiency of Ab-Initio Total Energy Calculations for Metals and Semiconductors Using a Plane-Wave Basis Set. *Comput. Mater. Sci.* **1996**, *6*, 15–50.

(30) Perdew, J. P.; Burke, K.; Ernzerhof, M. Generalized Gradient Approximation Made Simple. *Phys. Rev. Lett.* **1996**, *77*, 3865–3868.

(31) Togo, A.; Tanaka, I. First Principles Phonon Calculations in Materials Science. *Scr. Mater.* **2015**, *108*, 1–5.

(32) Symmetry analyses were carried out using the spglib library written by A. Togo, http://atztogo.github.io/spglib.

(33) Harris, D. C.; Bertolucci, M. D. *Symmetry and Spectroscopy: An Introduction to Vibrational and Electronic Spectroscopy*; Dover Publications, 1978.

(34) Nakamoto, K. *Infrared and Raman Spectra of Inorganic and Coordination Compounds, Theory and Applications in Inorganic Chemistry*; Wiley, 2008.

(35) Pistorius, C. W. F. T. The Harmonic Vibration Problem of the Cubic XY_8 Molecule. *Bull. Soc. Chim. Belg.* **1959**, *68*, 630–642.

(36) Powell, R. C. *Symmetry, Group Theory, and the Physical Properties of Crystals*; Springer New York, 2010.

(37) Hofmeister, A. M.; Campbell, K. R. Infrared Spectroscopy of Yttrium Aluminum, Yttrium Gallium, and Yttrium Iron Garnets. *J. Appl. Phys.* **1992**, *72*, 638–646.

(38) Bachmann, V.; Ronda, C.; Meijerink, A. Temperature Quenching of Yellow Ce^{3+} Luminescence in YAG:Ce. *Chem. Mater.* **2009**, *21*, 2077–2084.

(39) Gharaee, L.; Erhart, P.; Hyldgaard, P. Finite-Temperature Properties of Nonmagnetic Transition Metals: Comparison of the Performance of Constraint-Based Semilocal and Nonlocal Functionals. *Phys. Rev. B* **2017**, *95*, 085147.

(40) Raudonyte, E.; Bettentrup, H.; Uhlich, D.; Sakirzanovas, S.; Opuchovic, O.; Tautkus, S.; Katelnikovas, A. On the $Ce^{3+} \rightarrow Cr^{3+}$ Energy Transfer in $Lu_3Al_5O_{12}$ Gar- nets. *Opt. Mater.* **2014**, *37*, 204–210.

(41) Shannon, R. D. Revised Effective Ionic Radii and Systematic Studies of Interatomic Distances in Halides and Chalcogenides. *Acta Crystallogr.* **1976**, *32*, 751–767.

(42) Seijo, L.; Barandiarán, Z. 4*f* and 5*d* Levels of Ce^{3+} in D_2 8-fold oxygen coordination. *Opt. Mater.* **2013**, *35*, 1932–1940.

(43) Chiang, C.-C.; Tsai, M.-S.; Hon, M.-H. Luminescent Properties of Cerium-Activated Garnet Series Phosphor: Structure and Temperature Effects. *J. Electrochem. Soc.* **2008**, *155*, B517–B520.

(44) Birkel, A.; Denault, K. A.; George, N. C.; Doll, C. E.; Héry, B.; Mikhailovsky, A. A.; Birkel, C. S.; Hong, B.-C.; Seshadri, R. Rapid Microwave Preparation of Highly Efficient Ce^{3+}-Substituted Garnet Phosphors for Solid State White Lighting. *Chem. Mater.* **2012**, *24*, 1198–1204.

(45) Ivanovskikh, K. V.; Ogiegło, J. M.; Zych, A.; Ronda, C. R.; Meijerink, A. Luminescence Temperature Quenching for Ce^{3+} and Pr^{3+} *d-f* Emission in YAG and LuAG. *ECS J. Solid State Sci. Technol.* **2013**, *2*, R3148–R3152.

(46) Dexter, D. L.; Schulman, J. H. Theory of Concentration Quenching in Inorganic Phosphors. *J. Chem. Phys.* **1954**, *22*, 1063–1070.

(47) Ueda, J.; Tanabe, S.; Nakanishi, T. Analysis of Ce^{3+} Luminescence Quenching in Solid Solutions between $Y_3Al_5O_{12}$ and $Y_3Ga_5O_{12}$ by Temperature Dependence of Photoconductivity Measurement. *J. Appl. Phys.* **2011**, *110*, 053102.

(48) Ueda, J.; Dorenbos, P.; Bos, A. J. J.; Meijerink, A.; Tanabe, S. Insight into the Thermal Quenching Mechanism for $Y_3Al_5O_{12}:Ce^{3+}$ through Thermoluminescence Excitation Spectroscopy. *J. Phys. Chem. C* **2015**, *119*, 25003–25008.

(49) Robbins, D. J. The Effects of Crystal Field and Temperature on the Photoluminescence Excitation Efficiency of Ce^{3+} in YAG. *J. Electrochem. Soc.* **1979**, *126*, 1550–1555.

(50) Liu, J.; Wang, X.; Xuan, T.; Wang, C.; Li, H.; Sun, Z. $Lu_3(Al,Si)_5(O,N)_{12}:Ce^{3+}$ Phosphors with Broad Emission Band and High Thermal Stability for White LEDs. *J. Lumin.* **2015**, *158*, 322–327.

(51) Shao, Q.; Dong, Y.; Jiang, J.; Liang, C.; He, J. Temperature-Dependent Photoluminescence Properties of (Y, Lu)$_3$Al$_5$O$_{12}$:Ce^{3+} Phosphors for White LEDs Applications. *J. Lumin.* **2011**, *131*, 1013–1015.

(52) Dorenbos, P. Electronic Structure and Optical Properties of the Lanthanide Activated $RE_3(Al_{1-x}Ga_x)_5O_{12}$ (RE=Gd, Y, Lu) Garnet Compounds. *J. Lumin.* **2013**, *134*, 310–318.

(53) Hermus, M.; Phan, P.-C.; Duke, A. C.; Brgoch, J. Tunable Optical Properties and Increased Thermal Quenching in the Blue-Emitting Phosphor Series: $Ba_2(Y_{1-x}Lu_x)_5B_5O_{17}$:Ce^{3+} ($x = 0 - 1$). *Chem. Mater.* **2017**, *29*, 5267–5275.

(54) Shionoya, S.; Yen, W. M.; Yamamoto, H. *Phosphor Handbook*; CRC Press, 2006.

(55) Blasse, G.; Grabmaier, B. C. *Luminescent Materials*; Springer Berlin Heidelberg, 1994.

Graphical TOC Entry

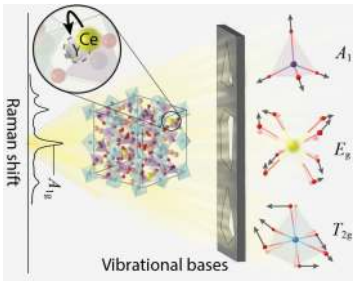

Supporting Information:

Understanding the Interactions Between Vibrational Modes and Excited State Relaxation in $Y_{3-x}Ce_xAl_5O_{12}$: Design Principles for Phosphors Based on 5*d*–4*f* Transitions

Yuan-Chih Lin[†], Paul Erhart[‡], Marco Bettinelli[¶], Nathan C. George[§,‖], Stewart F. Parker[⊥], and Maths Karlsson[*,†]

†Department of Chemistry and Chemical Engineering, Chalmers University of Technology, SE-412 96 Göteborg, Sweden
‡Department of Physics, Chalmers University of Technology, SE-412 96 Göteborg, Sweden.
¶Luminescent Materials Laboratory, University of Verona and INSTM, UdR Verona, 37134 Verona, Italy
§Department of Chemical Engineering, University of California, Santa Barbara, California 93106, United States
‖Mitsubishi Chemical Center for Advanced Materials, University of California, Santa Barbara, California 93106, United States
⊥ISIS Facility, STFC Rutherford Appleton Laboratory, Chilton, Didcot, Oxon OX11 0QX United Kingdom

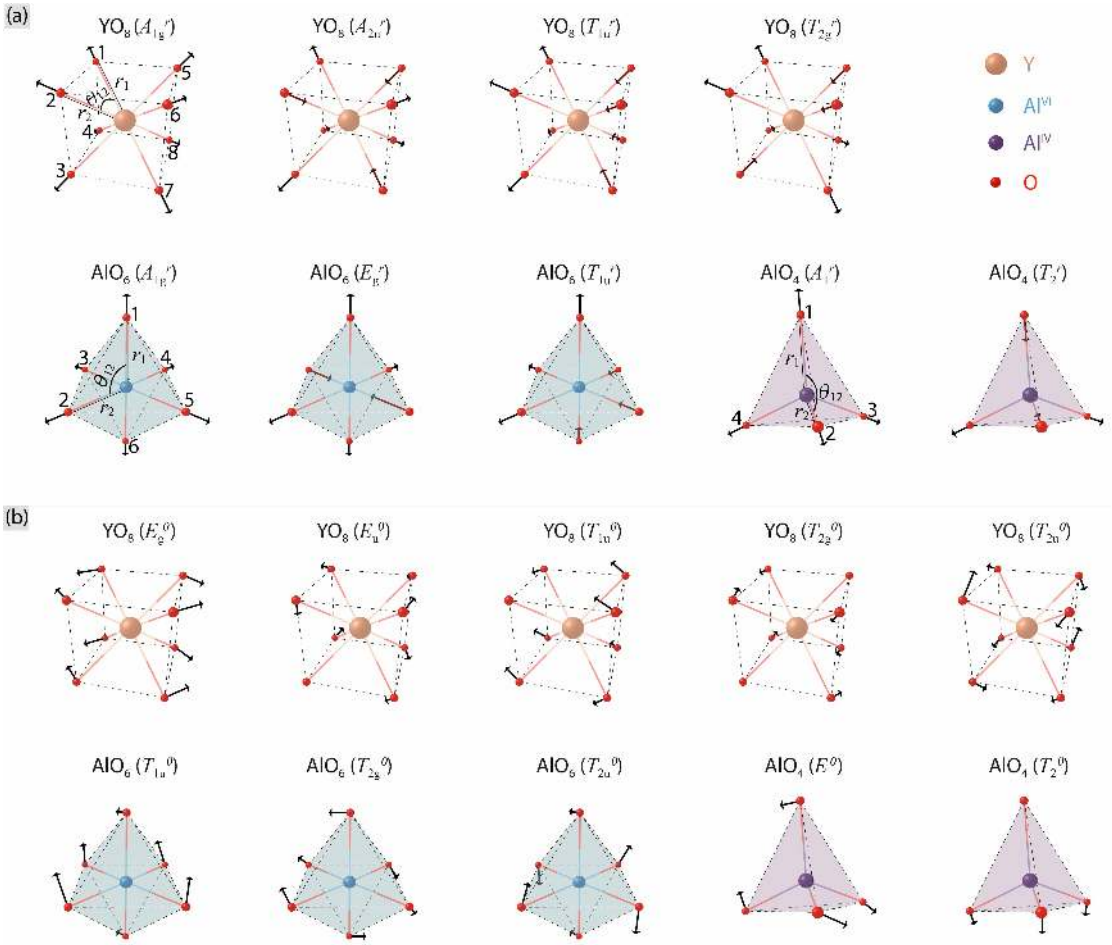

Figure S1 Symmetry coordinates, $|\eta\rangle$, for (a) stretching and (b) bending vibrations of cubic YO_8, octahedral AlO_6, and tetrahedral AlO_4 moieties. See Table S1 for mathematical expression of the symmetry coordinates.

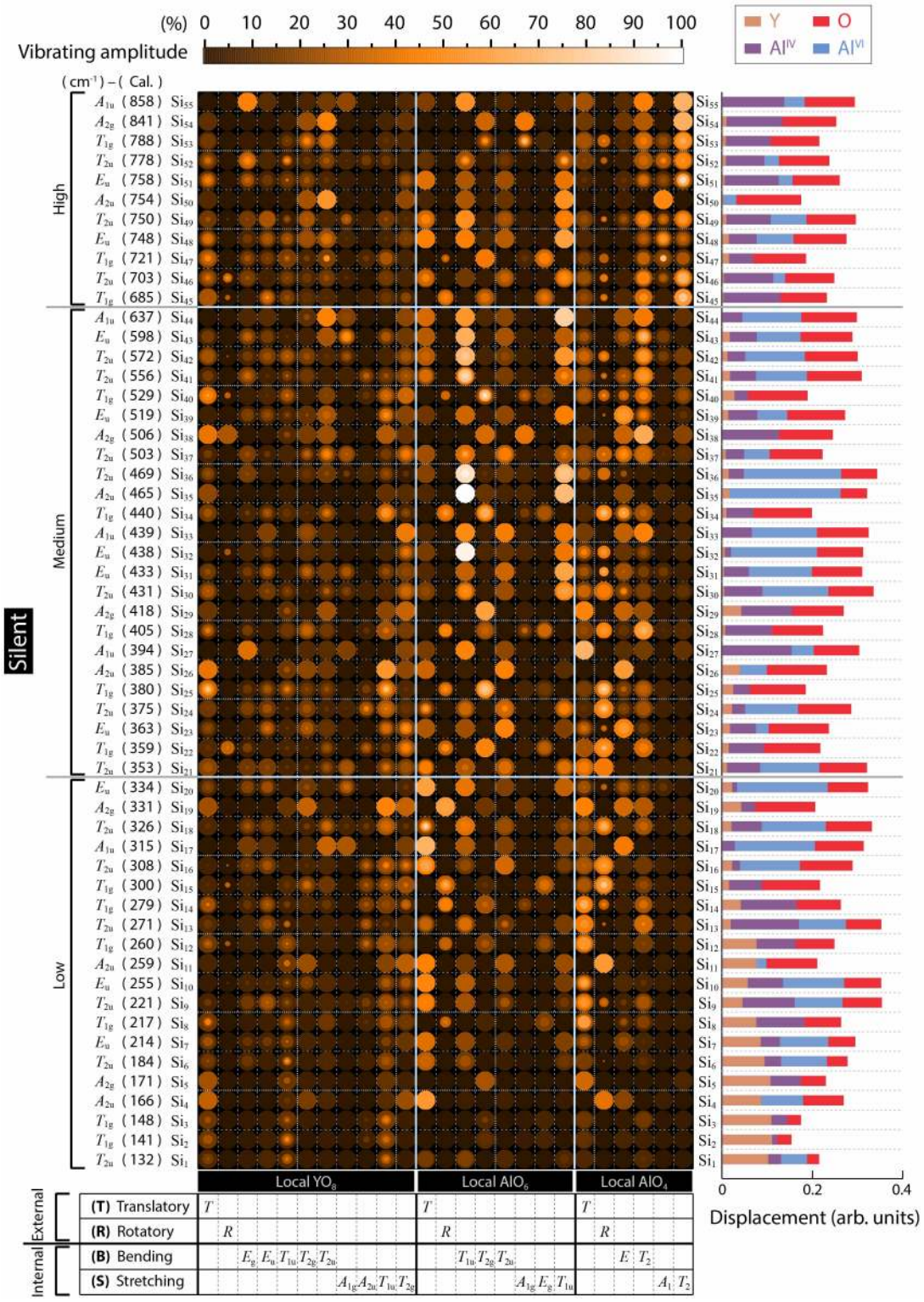

Figure S2 *Left:* full PDM for all optically silent modes of YAG. *Right:* averaged atomic displacements for the Y, Al^{VI}, Al^{IV}, and O atoms.

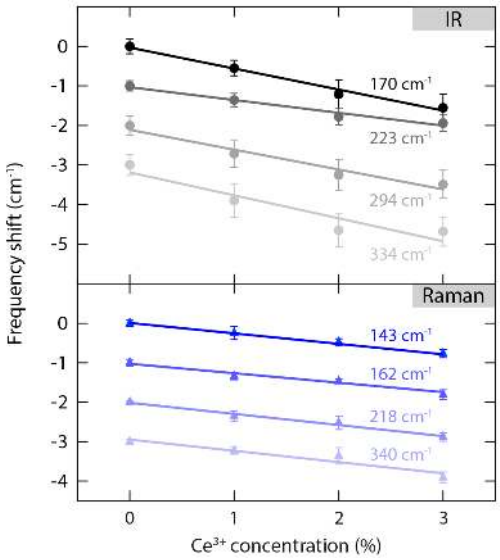

Figure S3 Vibrational frequency shift of YAG :z%Ce^{3+} upon increasing Ce^{3+} dopant concentration (z).

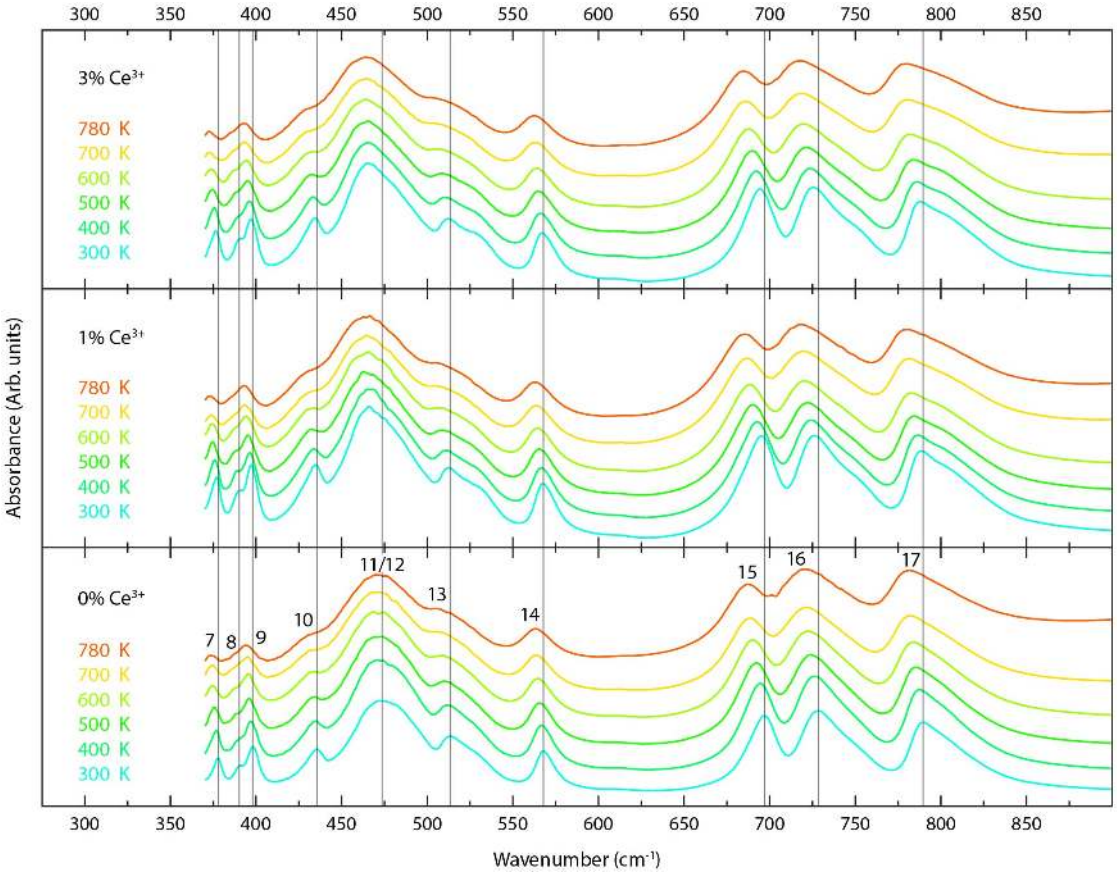

Figure S4 IR spectra of YAG :z%Ce^{3+} ($z = 0$, 1, and 3) in the temperature range of 300–780 K. Vertical lines are positioned at the maxima of the IR and Raman bands of YAG.

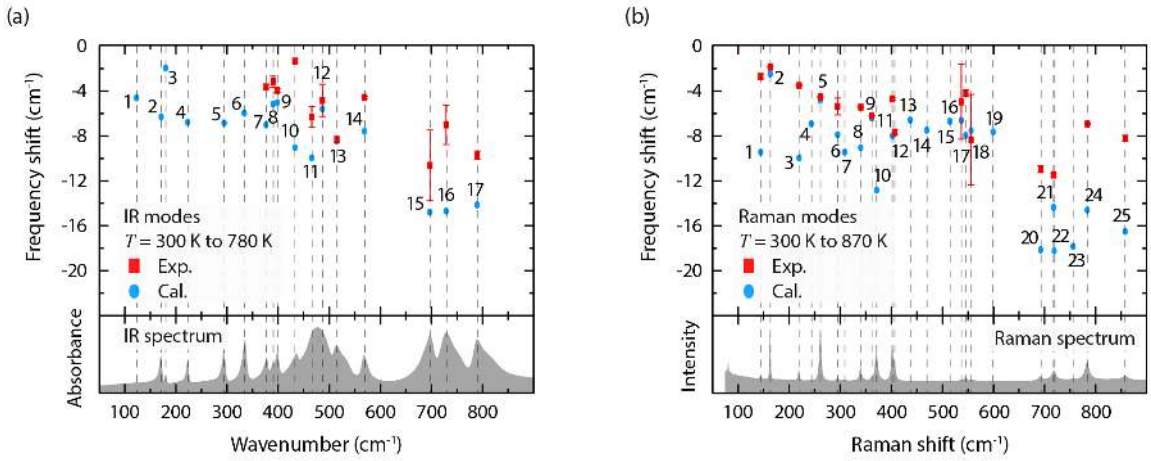

Figure S5 Experimental and calculated vibrational frequency shift of YAG upon increasing temperature (a) from 300 to 780 K for the IR modes and (b) from 300 to 870 K for the Raman modes.

Table S1 Mathematical description of the symmetry coordinates, $|\eta\rangle$, of cubic YO_8, octahedral AlO_6, and tetrahedral AlO_4 moieties, expressed in terms of the internal coordinates r (bonding length) and θ (bonding angle), *cf.* Figure S1. Degeneracy of symmetry coordinates is denoted by the superscripts $'$, $''$ and $'''$.

Displacement	Symmetry coordinate
Cubic YO_8	
Symmetric stretching	$A_{1g}^{r} = \frac{1}{2\sqrt{2}}\Delta(r_1 + r_2 + r_3 + r_4 + r_5 + r_6 + r_7 + r_8)$
Asymmetric stretching	$A_{2u}^{r} = \frac{1}{2\sqrt{2}}\Delta(r_1 - r_2 + r_3 - r_4 - r_5 + r_6 - r_7 + r_8)$
Asymmetric stretching	$T_{1u}^{'\,r} = \frac{1}{2\sqrt{6}}\Delta(3r_1 + r_2 - r_3 + r_4 + r_5 - r_6 - 3r_7 - r_8)$
Asymmetric stretching	$T_{1u}^{''\,r} = \frac{1}{2}\Delta(r_2 + r_3 - r_5 - r_8)$
Asymmetric stretching	$T_{1u}^{'''\,r} = \frac{1}{2\sqrt{3}}\Delta(r_2 - r_3 - 2r_4 + r_5 + 2r_6 - r_8)$
Stretching	$T_{2g}^{'\,r} = \frac{1}{2\sqrt{6}}\Delta(3r_1 - r_2 - r_3 - r_4 - r_5 - r_6 + 3r_7 - r_8)$
Stretching	$T_{2g}^{''\,r} = \frac{1}{2}\Delta(r_2 - r_3 - r_5 + r_8)$
Stretching	$T_{2g}^{'''\,r} = \frac{1}{2\sqrt{3}}\Delta(-r_2 - r_3 + 2r_4 - r_5 + 2r_6 - r_8)$
Symmetric bending	$E_{g}^{'\,\theta} = \frac{1}{2\sqrt{6}}\Delta(2\theta_{12} - \theta_{14} - \theta_{15} - \theta_{23} - \theta_{26} + 2\theta_{34} - \theta_{37} - \theta_{48} + 2\theta_{56} - \theta_{58} - \theta_{67} + 2\theta_{78})$
Symmetric bending	$E_{g}^{''\,\theta} = \frac{1}{2\sqrt{6}}\Delta(2\theta_{13} - \theta_{16} - \theta_{18} + 2\theta_{24} - \theta_{25} - \theta_{27} - \theta_{36} - \theta_{38} - \theta_{45} - \theta_{47} + 2\theta_{57} + 2\theta_{68})$
Symmetric twisting	$E_{u}^{'\,\theta} = \frac{1}{2\sqrt{6}}\Delta(2\theta_{13} - \theta_{16} - \theta_{18} - 2\theta_{24} + \theta_{25} + \theta_{27} - \theta_{36} - \theta_{38} + \theta_{45} + \theta_{47} - 2\theta_{57} + 2\theta_{68})$
Symmetric twisting	$E_{u}^{''\,\theta} = \frac{1}{2\sqrt{2}}\Delta(\theta_{16} - \theta_{18} - \theta_{25} + \theta_{27} - \theta_{36} + \theta_{38} + \theta_{45} - \theta_{47})$
Asymmetric bending	$T_{1u}^{'\,\theta} = \frac{1}{4}\Delta(2\theta_{12} + \theta_{14} + \theta_{15} + \theta_{23} + \theta_{26} - \theta_{37} - \theta_{48} - \theta_{58} - \theta_{67} - 2\theta_{78})$
Asymmetric bending	$T_{1u}^{''\,\theta} = \frac{1}{2}\Delta(\theta_{13} + \theta_{24} - \theta_{57} - \theta_{68})$
Asymmetric bending	$T_{1u}^{'''\,\theta} = \frac{1}{4}\Delta(\theta_{14} - \theta_{15} + \theta_{23} - \theta_{26} + 2\theta_{34} + \theta_{37} + \theta_{48} - 2\theta_{56} - \theta_{58} - \theta_{67})$
Bending	$T_{2g}^{'\,\theta} = \frac{1}{2}\Delta(\theta_{12} - \theta_{34} - \theta_{56} + \theta_{78})$
Bending	$T_{2g}^{''\,\theta} = \frac{1}{2}\Delta(\theta_{13} - \theta_{24} + \theta_{57} - \theta_{68})$
Bending	$T_{2g}^{'''\,\theta} = \frac{1}{2}\Delta(\theta_{14} - \theta_{23} - \theta_{58} + \theta_{67})$
Asymmetric twisting	$T_{2u}^{'\,\theta} = \frac{1}{4}\Delta(2\theta_{12} - \theta_{14} - \theta_{15} - \theta_{23} - \theta_{26} + \theta_{37} + \theta_{48} + \theta_{58} + \theta_{67} - 2\theta_{78})$
Asymmetric twisting	$T_{2u}^{''\,\theta} = \frac{1}{4}\Delta(-\theta_{14} + \theta_{15} - \theta_{23} + \theta_{26} + 2\theta_{34} - \theta_{37} - \theta_{48} - 2\theta_{56} + \theta_{58} + \theta_{67})$
Asymmetric twisting	$T_{2u}^{'''\,\theta} = \frac{1}{2\sqrt{2}}\Delta(\theta_{14} - \theta_{15} - \theta_{23} + \theta_{26} + \theta_{37} - \theta_{48} + \theta_{58} - \theta_{67})$

continued on next page

Table S1 *continued*

Octahedral AlO_6	
Symmetric stretching	$A_{1g}^{r} = \frac{1}{\sqrt{6}}\Delta(r_1 + r_2 + r_3 + r_4 + r_5 + r_6)$
Stretching	$E_{g}^{'\,r} = \frac{1}{2\sqrt{3}}\Delta(2r_1 - r_2 - r_3 - r_4 - r_5 + 2r_6)$
Stretching	$E_{g}^{''\,r} = \frac{1}{2}\Delta(r_2 - r_3 + r_4 - r_5)$
Asymmetric stretching	$T_{1u}^{'\,r} = \frac{1}{\sqrt{2}}\Delta(r_1 - r_6)$
Asymmetric stretching	$T_{1u}^{''\,r} = \frac{1}{\sqrt{2}}\Delta(r_2 - r_4)$
Asymmetric stretching	$T_{1u}^{'''\,r} = \frac{1}{\sqrt{2}}\Delta(r_3 - r_5)$
Asymmetric bending	$T_{1u}^{'\,\theta} = \frac{1}{4}\Delta(2\theta_{12} + \theta_{13} + \theta_{15} + \theta_{23} + \theta_{25} - \theta_{34} - \theta_{36} - \theta_{45} - 2\theta_{46} - \theta_{56})$
Asymmetric bending	$T_{1u}^{''\,\theta} = \frac{1}{2\sqrt{2}}\Delta(\theta_{13} - \theta_{15} + \theta_{23} - \theta_{25} + \theta_{34} + \theta_{36} - \theta_{45} - \theta_{56})$
Asymmetric bending	$T_{1u}^{'''\,\theta} = \frac{1}{4}\Delta(\theta_{13} + 2\theta_{14} + \theta_{15} - \theta_{23} - \theta_{25} - 2\theta_{26} + \theta_{34} - \theta_{36} + \theta_{45} - \theta_{56})$
Bending	$T_{2g}^{'\,\theta} = \frac{1}{2}\Delta(\theta_{12} - \theta_{14} - \theta_{26} + \theta_{46})$
Bending	$T_{2g}^{''\,\theta} = \frac{1}{2}\Delta(\theta_{13} - \theta_{15} - \theta_{36} + \theta_{56})$
Bending	$T_{2g}^{'''\,\theta} = \frac{1}{2}\Delta(\theta_{23} - \theta_{25} - \theta_{34} + \theta_{45})$
Asymmetric bending	$T_{2u}^{'\,\theta} = \frac{1}{4}\Delta(2\theta_{12} - \theta_{13} - \theta_{15} - \theta_{23} - \theta_{25} + \theta_{34} + \theta_{36} + \theta_{45} - 2\theta_{46} + \theta_{56})$
Asymmetric bending	$T_{2u}^{''\,\theta} = \frac{1}{2\sqrt{2}}\Delta(\theta_{13} - \theta_{15} - \theta_{23} + \theta_{25} - \theta_{34} + \theta_{36} + \theta_{45} - \theta_{56})$
Asymmetric bending	$T_{2u}^{'''\,\theta} = \frac{1}{4}\Delta(-\theta_{13} + 2\theta_{14} - \theta_{15} + \theta_{23} + \theta_{25} - 2\theta_{26} - \theta_{34} + \theta_{36} - \theta_{45} + \theta_{56})$
Tetrahedral AlO_4	
Symmetric stretching	$A_{1}^{r} = \frac{1}{2}\Delta(r_1 + r_2 + r_3 + r_4)$
Asymmetric stretching	$T_{2}^{'\,r} = \frac{1}{2\sqrt{3}}\Delta(3r_1 - r_2 - r_3 - r_4)$
Asymmetric stretching	$T_{2}^{''\,r} = \frac{1}{\sqrt{2}}\Delta(r_2 - r_3)$
Asymmetric stretching	$T_{2}^{'''\,r} = \frac{1}{\sqrt{6}}\Delta(r_2 + r_3 - 2r_4)$
Symmetric bending	$E^{'\,\theta} = \frac{1}{2\sqrt{3}}\Delta(2\theta_{12} - \theta_{13} - \theta_{14} - \theta_{23} - \theta_{24} + 2\theta_{34})$
Symmetric bending	$E^{''\,\theta} = \frac{1}{2}\Delta(\theta_{13} - \theta_{14} - \theta_{23} + \theta_{24})$
Asymmetric bending	$T_{2}^{'\,\theta} = \frac{1}{\sqrt{2}}\Delta(\theta_{12} - \theta_{34})$
Asymmetric bending	$T_{2}^{''\,\theta} = \frac{1}{\sqrt{2}}\Delta(\theta_{13} - \theta_{24})$
Asymmetric bending	$T_{2}^{'''\,\theta} = \frac{1}{\sqrt{2}}\Delta(\theta_{14} - \theta_{23})$

Table S2 Compilation of the Debye temperature θ_D (in units of Kelvin), of YAG with lattice constant a at the environmental temperatures of 300, 500 and 1200 K that is denoted by $a_{300\ K}$, $a_{500\ K}$, and $a_{1200\ K}$, respectively, where $a_{1200\ K} > a_{500\ K} > a_{300\ K}$. θ_D is derived from the mean-square-displacement $\langle u^2 \rangle$ through $\langle u^2 \rangle = \frac{3\hbar^2}{mk_BT}(\frac{1}{x^2})(1+\frac{x^2}{36}-\frac{x^4}{3600})$, where $x = \theta_D/T$ and m is the mass of the atom, see ref. S1 for details.

YAG	$a_{300\ K}$		$a_{500\ K}$		$a_{1200\ K}$	
Atoms	$\langle u^2 \rangle$ (Å^2)	θ_D (K)	$\langle u^2 \rangle$ (Å^2)	θ_D (K)	$\langle u^2 \rangle$ (Å^2)	θ_D (K)
Y	0.003891	362.28	0.006940	345.67	0.018951	322.27
Al^{VI}	0.003638	715.07	0.005930	691.74	0.014748	665.27
Al^{IV}	0.003406	742.58	0.005401	726.64	0.012932	710.88
O	0.004670	837.99	0.007407	811.02	0.017979	783.75
Average		740.03		716.63		691.75

References

(S1) Willis, B. T. M.; Pryor, A. W. *Thermal Vibrations in Crystallography*; Cambridge University Press, 1975.